



Contents lists available at ScienceDirect

Journal of the Mechanics and Physics of Solids

journal homepage: www.elsevier.com/locate/jmps

The influence of mean strain on the high-cycle fatigue of Nitinol with application to medical devices

Hengchu Cao^a, Ming H. Wu^a, Fei Zhou^a, Robert M. McMeeking^{b,c,d,e},
Robert O. Ritchie^{f,g,h,*}

^a Edwards Lifesciences, One Edwards Way, Irvine, CA 92614, USA

^b Materials Department, University of California, Santa Barbara, CA 93106, USA

^c Department of Mechanical Engineering, University of California, Santa Barbara, CA 93106, USA

^d School of Engineering, University of Aberdeen, King's College, Aberdeen, AB24 3UE, UK

^e INM – Leibniz Institute for New Materials, Campus D2 2, 66123 Saarbrücken, Germany

^f Materials Sciences Division, Lawrence Berkeley National Laboratory, Berkeley, CA 94720, USA

^g Department of Materials Science & Engineering, University of California, Berkeley, CA 94720, USA

^h Department of Mechanical Engineering, University of California Berkeley, CA 94720, USA



ARTICLE INFO

Article history:

Received 17 December 2019

Revised 25 April 2020

Accepted 10 June 2020

Available online 18 June 2020

Keywords:

Nitinol
Superelastic
Shape memory
High-cycle
Fatigue
Reliability
Goodman
Weibull
Implant
Cardiovascular

ABSTRACT

One of the contentious issues associated with the high-cycle fatigue of Nitinol, a nominally equiatomic alloy of nickel and titanium, is the claim that increasing the applied mean strain can *increase*, or at least have no negative impact, on the fatigue lifetime, in conflict with reported behavior for the vast majority of other metallic materials. To investigate this in further detail, cyclic fatigue tests in bending were carried out on electropolished medical grade Nitinol at 37 °C for lives of up to 400 million cycles of strain involving various levels of the mean strain. A constant life model was developed through statistical analysis of the fatigue data, with 90% reliability at a confidence level of 95% on the effective fatigue strain. Our results show that the constant life diagram, a plot of strain amplitude versus mean strain, is monotonic yet nonlinear for lives of 400 million cycles of fatigue loading. Specifically, we find that in contradiction to the aforementioned claim, the strain amplitude limit *at zero mean strain* is 0.55% to achieve a 400 million cycle lifetime, at 90% reliability with 95% confidence; however, to achieve the same lifetime, reliability and confidence level in the presence of a 3% or more mean strain, *the required strain amplitude limit is decreased by over a factor of three* to 0.16%. Moreover, for mean strains from 3% to 7%, the strain amplitude limit that allows a 400 million cycle lifetime, at 90% reliability with 95% confidence, is ~ 0.16%, and essentially independent of mean strain. We conclude that the debatable claim that an increase in the applied mean strain can increase the fatigue life of Nitinol components is not supported by the current data.

© 2020 The Authors. Published by Elsevier Ltd.
This is an open access article under the CC BY license.
(<http://creativecommons.org/licenses/by/4.0/>)

* Corresponding author at: Department of Materials Science & Engineering, University of California, Berkeley, CA 94720, USA.
E-mail address: ritchie@berkeley.edu (R.O. Ritchie).

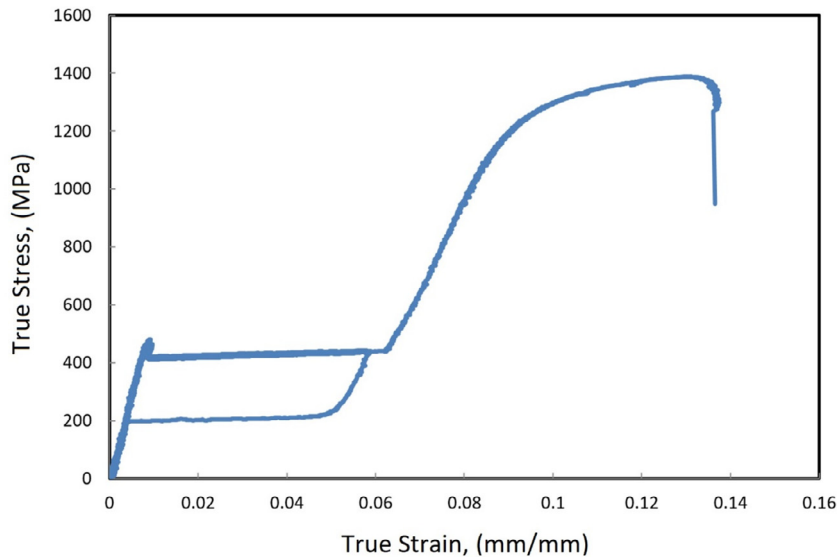


Fig. 1. A typical true stress-true strain curve obtained at 37 °C from a uniaxial tensile test of a superelastic Nitinol specimen with a transformation temperature, A_f , of approximately 15 °C. The test was performed following ASTM F2516 at a loading rate of 0.1 mm/s to 6% engineering strain for a specimen of length 10 mm. The specimen was then unloaded to zero load and then reloaded to final failure. A group of 9 specimens was tested with the average of the stress from the 9 specimens at a given strain used to derive the elastic and superelastic constitutive parameters based on the [Auricchio and Taylor \(1997\)](#) model.

1. Introduction

Nitinol (NiTi) is a shape memory alloy composed of nominally equiatomic proportions of nickel and titanium, with metallurgical characteristics and properties associated with an austenite-martensite phase transition from a cubic lattice to a monoclinic one ([Duerig et al., 1990](#); [Otsuka and Ren, 2005](#)). In addition to its thermomechanical behavior consistent with its shape-memory characteristics, at selected temperatures Nitinol is superelastic (also termed pseudoelastic), enabling large recoverable strains through combinations of the austenite-martensite phase transformation and twinning/detwinning of the martensite. Such behavior is associated with stress-strain hysteresis loops ([Pelton et al., 2000](#)). In some technologies it is the shape-memory properties that are exploited, with examples being aircraft fuel line couplings and actuator springs ([Robertson et al., 2012](#)). In medical applications, conversely, it is predominantly the superelastic phenomena of Nitinol that are utilized, as it enables transcatheter delivery followed by spontaneous expansion of the device into the patient's anatomy ([Duerig et al., 1999](#); [Stöckel et al., 2004](#)). Examples of such devices made from Nitinol are self-expanding arterial stents ([Pelton et al., 2008](#)), self-expanding inferior vena cava filters ([Grassi, 1991](#)), and self-expanding heart valves ([Lanz et al., 2019](#)).

A uniaxial tensile stress-strain curve for a superelastic (medical grade) Nitinol at 37 °C is shown in [Fig. 1](#). The material is thermomechanically treated so that its austenite finish temperature, A_f , is ~15 °C, *i.e.*, sufficiently below the body temperature to ensure superelasticity under physiological service conditions. For medical implant applications, one carries out the test at 37 °C to fully characterize the mechanical response of the material applicable to a long-term service environment inside the human body.

Once Nitinol medical implants are delivered into the human body, almost all devices experience the cyclic imposition of a wide range of deformations, caused by various sources such as the cardiac cycle ([Milnor, 1982](#)), respiration ([Murphy et al., 2008](#)), Valsalva and similar maneuvers ([Laborda et al., 2014](#)) and the distortions of organs and vessels caused by activities such as walking ([Cheng et al., 2006](#)). As in all metal alloys, this raises the possibility that failure will occur by fatigue fracture ([Robertson et al., 2012](#); [Suresh, 1998](#)). Such fractures have been identified in implanted arterial stents ([Pelton et al., 2008](#)) and in implanted inferior vena cava filters ([Hull and Robertson, 2009](#)), both made of Nitinol. Reliable fatigue life data for medical grade Nitinol are thus of paramount importance to enable safe design and reliable lifetime assessment of medical implants made from this alloy. One of the contentious issues associated with the high-cycle fatigue of Nitinol is the claim that increasing the applied mean strain can *increase* the life ([Pelton et al., 2008](#)). As this contradicts reported fatigue behavior for virtually all other metallic materials, the aim of the current work is to critically examine the role of the mean strain using a new test method to determine fatigue strain-life data, utilizing a novel bending specimen, with experimental validation of the fatigue strain. The ultimate objective is to provide a reliable constant life diagram for Nitinol in terms of strain amplitude versus mean strain. Furthermore, we note that most medical implants contain some local regions in the design in which the Nitinol operates at a substantial *R*-ratio during strain cycling, where *R* is defined as the minimum strain

divided by the maximum strain. Therefore, the constant life diagram that we seek encompasses mean strains consistent with such substantial R -ratios.

We note that it is common to define the so-called fatigue endurance limit as the stress or strain amplitude at zero mean stress or strain at which all specimens tested survive for at least 10 million cycles without fracture. However, we observe that medical device applications usually demand a life of 10 years of survival without fracture. At 72 beats per minute, 10 years of the cardiac cycle is equivalent to just under 400 million cycles of loading of a prosthetic heart valve or of any other device that is deformed cyclically by the heart. At 15 breaths per minute, 10 years of respiration is equivalent to just under 80 million cycles of deformation of an inferior vena cava filter, or of any other device that is loaded by the respiratory cycle. This raises the question of whether an endurance limit for Nitinol calibrated to 10 million cycle fatigue data is an accurate predictor of a safe fatigue life for 100 or 400 million cycles of deformation; this is an additional objective of the research presented in this paper.

2. Nitinol fatigue life data

There are many data in the literature addressing the fatigue properties of Nitinol, as reviewed recently by Robertson et al. (2012). As noted in that review, much of the early published data was affected by poor processing control in the production of the NiTi alloys involved. As noted by Robertson et al. (2012), modern Nitinol alloys used in medical implants tend to receive extensive thermomechanical processing treatments, producing microstructures rather different from those in materials generated in the past by full annealing or with long duration thermal treatments at high temperature. Clearly, this situation limits the utility of some of the older data for the fatigue life of Nitinol alloys in the literature; as such, we simply refer to Robertson et al. (2012) for a summary of the relevant information.

When we consider modern data for the fatigue life of medical grade Nitinol, we find very few that are amenable to simple interpretation. Furthermore, the situation is complicated by the characteristics of Nitinol's stress-strain curve as shown in Fig. 1. In particular, for the range of stresses in which the material is generally utilized, there is no unique state corresponding to a given stress level. Only at stresses below and above the hysteresis loop (Fig. 1) can one identify unique states of the material; at stress levels encompassing the hysteresis loop there are at least two states corresponding to each value of stress, one at the left end of the hysteresis loop and the other at the right end. In fact, the situation is even more complicated because the partial transformation of material from austenite to martensite and the corresponding partial reverse transformation means that for any given stress level in Fig. 1, there are an infinity of states of the material corresponding to all points at that stress level within the hysteresis loop. For this reason, there is a common perception that, for the purpose of fatigue properties, it is better to characterize the state of the Nitinol in terms of strain. Therefore, fatigue data for Nitinol, e.g. so called S - N (or Wöhler) curves and Goodman-Haigh (or simply Goodman) diagrams, are usually given in terms of strain amplitude and mean strain and not in the usual terms of stress amplitude and mean stress. For the present paper we will follow this convention. However, we must point out that the situation is no better with regard to strain, as, within the range of strain encompassing the hysteresis loop in Fig. 1, there are at least two states of the material for any given strain level, one on the lower plateau of the loop and one on the upper plateau. Furthermore, partial transformation of the material also leads to there being an infinity of states within the hysteresis loop for any given level of strain. The best that can be said is that, due to the flatness of the upper and lower plateaus of the hysteresis loop, for any given level of strain the extent of variation of the state of the material is likely to be less than for any given level of stress. For this reason, we find the use of strain to characterize fatigue properties of Nitinol to be more satisfactory than the use of stress, e.g. in S - N curves and Goodman diagrams.

The ideal situation would be one where the state of Nitinol is completely characterized by its history of stress and strain, and where given data for its fatigue properties are considered to be only relevant to material that has experienced that specific stress and strain history. The importance of this can be understood based on the realization that austenitic Nitinol is essentially a different material from martensitic Nitinol, and thus these two phases of Nitinol can be expected to have different fatigue properties, as pointed out by Robertson et al. (2012). Such a feature is observed in practice, where fatigue data for Nitinol in the martensitic range is known to be rather different from those on the austenitic range (Robertson et al., 2012). Thus, if we consider any given sample of Nitinol to be a mixture of austenite and martensite, with the mass fraction of martensite varying from 0 to 1, the appropriate way to characterize the fatigue data of Nitinol would be to determine them for a given mass ratio of martensite to austenite, and only consider a given set of fatigue data to be relevant for the mass ratio for which it was determined. While this concept is attractive in principle, the difficulty is that strain cycling itself can cause the mass ratio of austenite to martensite to go through cycles of variation, as will occur if the mean strain in the fatigue process is above the value that initiates the austenite to martensite transformation and the strain amplitude is large in magnitude. Superimposed on this phenomenon is the feature that the microstructure of the phase mixture of Nitinol is dependant on the strain history, e.g., whether the transformation is driven by tension or compression. Thus, in many cases of relevance to applications of Nitinol, it is impossible to hold the state of the material fixed during strain cycling.

With the above considerations in mind, we now briefly review available fatigue data for Nitinol, with a focus on medical grade materials. Throughout this paper, we will follow the general convention for defining fatigue testing parameters, e.g. as defined by Hertzberg (1996), using the terminology strain amplitude, ε_a , defined as:

$$\varepsilon_a = \frac{\varepsilon_{\max} - \varepsilon_{\min}}{2} \quad (1)$$

where ε_{\max} and ε_{\min} are, respectively, the maximum and minimum strain experienced during strain cycling; in this paper, both are taken to be axial strains parallel to the maximum tensile principal stress direction, as noted above. However, we use the terminology alternating strain and strain amplitude interchangeably. Additionally, the mean strain is defined as:

$$\varepsilon_m = \frac{\varepsilon_{\max} + \varepsilon_{\min}}{2} \quad (2)$$

The R -ratio is thus given by:

$$R = \frac{\varepsilon_{\min}}{\varepsilon_{\max}} \quad (3)$$

It should be noted that the above definitions for the strain amplitude and the mean strain are only strictly applicable to proportional loading during cyclic fatigue. In an actual device with a complex geometry and combined (mixed-mode) loading conditions, proportional loading rarely occurs. In such a situation, more elaborate analysis is needed to compute the correct mean strain and strain amplitude. For multiaxial loading, non-proportional loading or situations involving residual stress, a general procedure is described by [Tripathy et al. \(2019\)](#). In all cases, the values of ε_{\min} and ε_{\max} are algebraic minimum and maximum strain value defined on the local material coordinate projected along a particular direction that is normal to a so-called critical plane for the most likely fatigue crack propagation. This convention overcomes the challenge with a fixed global coordinate system in typical static finite element analysis.

We first, address the fatigue life of alloys processed by methods involving a long duration thermal treatment at high temperature and then fatigue tested at a mean strain of zero ($R = -1$). As an example, we cite the results of [Kim and Miyazaki \(1997\)](#) and [Miyazaki et al. \(1999\)](#) who carried out rotary bend tests at zero mean strain out to 10^6 cycles at temperatures of 20 °C, 50 °C and 80 °C on Ni_{50.9}Ti_{49.1} wire that was 30% cold drawn and aged at 400 °C for 1 h, resulting in an austenite finish temperature, A_f , of 40 °C. These authors concluded that lower test temperatures resulted in longer fatigue lives at a given strain amplitude, although, in the long-life regime, there was a negligible difference among the results taken at different temperatures at strain amplitudes less than 1%. These data show that long lives exceeding $\sim 10^4$ cycles are obtained at the higher two test temperatures only when the strain amplitude is elastic, meaning that the alternating strain remains below the martensite start strain, ε_{MS} , at which transition from austenite to martensite commences. In the stress-strain curve shown in [Fig. 1](#), this is the strain at which the linear elastic response through the origin changes to the segment of the curve that forms the upper plateau of the hysteresis loop. At strain amplitudes above ε_{MS} , the fatigue life degrades to below 10^4 cycles. However, it should be pointed out that the strain amplitude to give a life of 10^3 cycles is considerably greater than 1%, whereas in most other metal alloys a fatigue life of 10^3 cycles can generally be associated with an alternating strain of 1%. [Robertson et al. \(2012\)](#) observe that many, if not all, Nitinol alloys exhibit a strain amplitude much greater than 1% when associated with a fatigue life of 10^3 cycles.

Fatigue results for superelastic Nitinol wire produced by more modern practice, in which continuous thermomechanical treatment is utilized leading to an austenite finish temperature, A_f , of 10 °C, show rotary bend test results for Ni_{50.8}Ti_{49.2} at zero mean strain in the long-life regime at 22 °C ([Reinoehl et al., 2000](#); [Sheriff et al., 2004](#); [Wick et al., 2004](#)) similar to those obtained by [Kim and Miyazaki \(1997\)](#) and [Miyazaki et al. \(1999\)](#). As in the latter data, the long-life regime involves a purely elastic response, with the strain amplitude, ε_a , less than the martensite start strain, ε_{MS} . In this state, the fatigue life increases rapidly as the strain amplitude is reduced; at a strain amplitude of $\sim 0.6\%$ the fatigue life is around 10^7 cycles, whereas at a strain amplitude of $\sim 0.65\%$ the fatigue life has fallen to around 10^5 cycles. Interestingly, the data for these continuously thermomechanically processed Nitinol alloys show that for $2\% < \varepsilon_a < 4\%$ there is a constant minimum life of approximately 1800 cycles associated with strain amplitudes that are large enough to convert the material completely from austenite to martensite and completely back again to austenite. The phenomenon of a constant minimum life in the range $2\% < \varepsilon_a < 4\%$ seems to be associated with the fact that the fatigue properties of pure martensite are superior to those of both pure austenite and partial mixtures of austenite and martensite. Thus, once pure martensite is being formed during strain cycling, the fatigue life in terms of number of cycles to failure rises rapidly towards that of thermal martensite ([Robertson et al., 2012](#)). In the intermediate regime, with strain amplitudes ranging from approximately 0.65% to 2% and lives ranging from 1800 cycles to approximately 10^5 cycles, where partial transformation from austenite to martensite is occurring during strain cycling, the fatigue life rises as the strain amplitude is reduced. However, the slope of these data, when the logarithm of the strain amplitude is plotted against the number of cycles to failure, is steeper than that prevailing at longer lives in the purely elastic regime. As a result, in this regime at a strain amplitude of 2% the fatigue life is 1800 cycles, whereas when the strain amplitude is reduced to approximately 0.65% the fatigue life rises to around 10^5 cycles.

[Wick et al. \(2004\)](#) compared data from [Reinoehl et al. \(2000\)](#) and [Sheriff et al. \(2004\)](#) to study the effect of electropolishing of the wires tested for their fatigue properties. They noted that electropolishing leads to a slight but statistically significant increase in the fatigue life in the low-cycle regime (cycles to failure $N_f < 10^3$), but no statistically significant improvement in the high-cycle regime.

When the effect of a nonzero mean strain on fatigue life is considered, the situation becomes more complex. Data show that strain-life curves have a fairly conventional appearance, with fatigue life increasing monotonically as the strain amplitude is reduced at a given nonzero mean strain ([Robertson et al., 2012](#)). However, the form of constant life (Goodman-type) diagrams, in which the strain amplitude is plotted versus mean strain for a constant life in terms of a given number of cycles, N_f , is more complicated than that found to be the case with many structural alloys. [Tabanlı et al. \(1999, 2001\)](#) performed fatigue tests on tubular specimens of superelastic Ni_{50.6}Ti_{49.4} subjected to axial strain at various values of mean strain ranging

from 0.25% to 9.3%, where the latter is well beyond the strain necessary to convert austenite entirely to martensite. Some of the tests were carried out at a temperature of 22 °C for materials having A_f ranging from -6 °C to -3 °C. Longer fatigue lives were found for tests at low mean strain, allowing them to cycle entirely within the austenite range, and for tests at high mean strain, where the material cycled purely within the martensite range. At intermediate mean strains, where the material was forced to transition between austenite to martensite and *vice versa* during strain cycling, the fatigue lives were shorter. Broadly speaking, the data of Tabanli et al. (1999, 2001) are consistent with the concept that increases in the mean strain decrease the fatigue life at a given strain amplitude, disrupted by the feature that the fatigue life of pure martensite is superior to that of austenite or mixtures of austenite and martensite. An alternative viewpoint, expressed by Tabanli et al. (1999, 2001), is that poor fatigue lives are associated with strain-driven phase transitions, whereas good fatigue lives arise from strain cycling within a single-phase regime. However, their data were obtained at a temperature that is somewhat higher compared to A_f than is often the case in the application of medical Nitinol alloys. In addition, it would appear that, for tests in which phase transitions were induced, strain cycling was initiated on the upper plateau of the stress-strain hysteresis loop, whereas medical applications tend to motivate strain cycling initiated on the lower plateau after prior overstraining (Robertson et al., 2012; Duerig et al., 1999; Stöckel et al., 2004; Pelton et al., 2008). Furthermore, the number of cycles to failure in the tests of Tabanli et al. (1999, 2001) was quite low compared to the number of cycles medical Nitinol alloys are expected to survive *in vivo*; in other words, the strain amplitudes in their tests were excessive compared to what is likely to be allowable in a Nitinol implant. These features mean that these data are not as applicable to practical component situations as might otherwise be the case. However, as a consequence of their results, Tabanli et al. (1999, 2001) concluded that conventional constant life diagrams of the Goodman or Soderberg type (Suresh, 1998; Mitchell, 1996) are not usable for Nitinol due its lack of a monotonic decrease in strain amplitude versus mean strain at constant life. This point of view has become widespread throughout the Nitinol fatigue community.

Tolomeo et al. (2000) observed contrasting behavior in a medical grade Nitinol having an austenite finish temperature, A_f , of 28 °C where fatigue tests were carried out at 37 °C. They constructed constant life plots for cycles to failure, N_f , equal to 10^6 , and found that, for such a life, the strain amplitude at mean strains from 0.5% to 6% had to be much less than the value obtained at $N_f = 10^6$ by Kim and Miyazaki (1997) at zero mean strain. However, Tolomeo et al. (2000) found that the best performance was obtained at intermediate mean strains of ~3% whereas fatigue durability, other than for zero mean strain, degraded for mean strains greater and less than 3%. Nevertheless, the constant life plot in the space of strain amplitude versus mean strain was found to be non-monotonic, and thus would seem to confirm that Goodman or Soderberg diagrams are not appropriate for Nitinol. It should be noted that the complexity of the stent unit cell used by Tolomeo et al. (2000) for their tests required data analysis by finite element calculations based on a constitutive law for superelastic behavior of Nitinol. However, the specimens, prior to fatigue testing, were stretched to induce strains of 6% and then relaxed to the desired mean strain level to be imposed during the fatigue test; thus, the cycling that occurred in cases other than for 6% mean strain commenced from the lower plateau of the superelastic stress-strain curve after overstraining, or from its purely elastic segment if the mean strain upon strain cycling was low enough.

Morgan et al. (2003), using a Nitinol wire having A_f of 12 °C, conducted fatigue tests in Ringer's solution at 38 °C and derived similar results to those of Tolomeo et al. (2000). Specifically, they found that the fatigue life increased with increasing mean strain from 2% to 6% for strain amplitudes that ranged from 0.5% to 3%. In these tests there was no overstraining before strain cycling, and thus, with regard to the mean strain level motivating the austenite/martensite transformation, the strain cycling commenced from the upper plateau of the superelastic stress-strain curve without prior overstraining.

Using a strategy similar to that of Tolomeo et al. (2000), Pelton et al. (2008) and Pelton et al. (2003) undertook fatigue tests on laser-machined strut specimens having a diamond shape, a configuration similar to unit cells in stents. Their tests were carried out to 10^7 cycles at 37 °C on $\text{Ni}_{50.8}\text{Ti}_{49.2}$ having $A_f = 29$ °C, with an initial compression step to 5% bending strain followed by extension to the targeted mean strain for the fatigue test. Thus, strain cycling commenced, after prior overstraining, from the unloading, lower plateau of the hysteresis loop in the superelastic stress-strain curve, or from the purely elastic line if the mean strain was low enough. As in the case of the results of Tolomeo et al. (2000), the data of Pelton et al. (2003, 2008) were interpreted through use of finite element analysis utilizing a constitutive law for superelastic Nitinol, with Pelton et al. (2008) providing some detail on how strain amplitudes and mean strains were calculated. We note that the methods used in these calculations are suspect, and we will return to this point below. From their analysis, Pelton et al. (2003, 2008) found that their constant life plot at $N_f = 10^7$ for strain amplitude versus mean strain was broadly monotonic. For this life, their data showed a strain amplitude of 0.4% at zero mean strain, rising to a strain amplitude of 0.8% at a mean strain of 4%; however, it should be noted that there was a range of lower mean strain (0 to 1%) in which the data were not monotonic, but the differences in strain amplitude in this segment were only 0.1%. Pelton (2011) later augmented these data with results obtained from 'dogbone' specimens, laser-machined from thermomechanically processed tube of the same Nitinol, and then axially pre-strained to 9% before relaxation to the target mean strain for the fatigue test (Robertson et al., 2012). Taken by themselves, the data from the 'dogbone' specimens give a constant life diagram for strain amplitude versus mean strain that is monotonic at a life of $N_f = 10^7$, but with the strain amplitude being constant at low mean strain up to 3% and falling at high mean strain above 7%. When combined with the data from the diamond strut specimens, the constant life diagram that arises for a life of $N_f = 10^7$ has a rather complicated, non-monotonic construction (Robertson et al., 2012; Pelton, 2011).

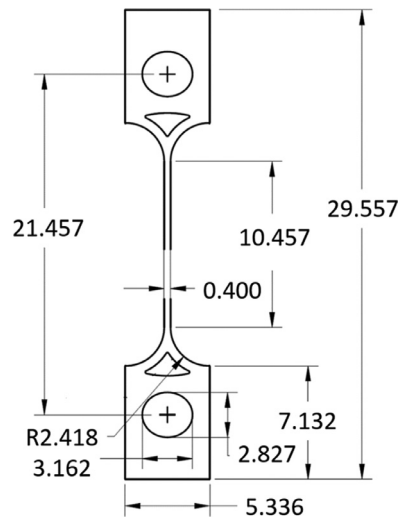


Fig. 2. Flat pattern dimensions (in mm) of the Nitinol fatigue specimen in the as-cut configuration. The long dimension of the specimen is parallel to the axis of the tube from which the specimen is cut, and the dimensions for the transverse directions are flat dimensions developed from the outer tube surface onto a flat plane.

We note that in additional work, [Pelton et al. \(2008\)](#) analysed fatigue tests on stents and overlaid the data for $N_f = 10^7$ on the constant life plot obtained from their work with diamond strut specimens. They found broad consistency between the two data sets and declared that the Goodman constructions ([Pelton et al., 2003, 2008](#)) traditionally used for a linear elastic constant life diagrams are invalid for superelastic Nitinol and that mean strain had a beneficial impact on the fatigue limit strain, except at extremely high mean strains exceeding 8%. They further attributed the improved fatigue resistance at high mean strain to purported higher fatigue resistance of the martensite phase ([Pelton et al., 2008; Pelton, 2011](#)).

3. Materials and experimental methods

Fatigue test specimens were laser cut from Nitinol tube, with a 10 mm outside diameter and a 0.41 mm thickness, having a composition $Ti_{50.7}Ni_{49.3}$ with an austenite start temperature (A_s) of -15°C , as measured from a fully annealed sample using differential scanning calorimeter (Pyris-1, PerkinElmer, MA). To ensure good fatigue performance of the material, we imposed more stringent requirements than those stated in ASTM Standard F2063¹ with regard to acceptance criteria for ceramic inclusions. The dimensions for the as-cut shape sample were defined by the flat pattern, as is often the practice in endovascular devices made from tubular raw material, and are shown in [Fig. 2](#). The long dimension of the specimen was parallel to the axis of the tube from which the specimen was cut, such that there was transverse curvature. After laser cutting, the specimen was deburred, shape-set, micro-blasted and electropolished. Shape-setting was performed by first inserting specimens in blanks in a plate, where the blanks had the shape defining the outer perimeter geometry of the finished specimen. Shape-setting was then achieved by immersing the tool in a fluidized bath at a temperature of 510°C for 10 min, and then quenching in water at room temperature, resulting in an austenite finish temperature, A_f , ranging from 15°C to 18°C . As a consequence of these procedures, each fatigue specimen was identical in shape with a uniform, curved gauge section. Manual micro-blasting with fine ceramic particles was then carried out to remove any oxide layer and to achieve uniform dimensions in the gauge section prior to electropolishing. The specimens were electropolished to achieve final dimensions in the gauge section, as shown in [Fig. 3](#).

The post-electropolishing dimensions of the fatigue specimens were measured using a Nikon system (Nikon NEXIV VMR-3020). The specimen gauge width was measured at 10 evenly spaced locations and recorded for each specimen to ensure uniformity. In addition, the specimen thickness in the gauge section was measured by a micrometre and recorded. Finally, the gauge section of the specimens was inspected visually at 10X and 50X (Nikon Stereomicroscope SMZ800) for any surface flaws or defects such as pits, divots, roughness, scratches, microcracks or sharp edges.

A Perkin-Elmer Pyris-1 differential scanning calorimeter (DSC) was used to verify that the austenite finish temperature, A_f , for the fatigue specimens processed in multiple batches was within the range specified above. Uniaxial tensile tests were performed on an Instron 3366 testing machine (Norwood, MA), equipped with an air-circulated environmental chamber, to

¹ ASTM F2063-18, "Standard Specification for Wrought Nickel-Titanium Shape Memory Alloys for Medical Devices and Surgical Implants," ASTM International, West Conshohocken PA (2018).

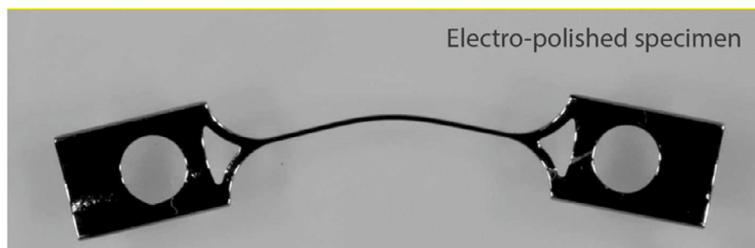
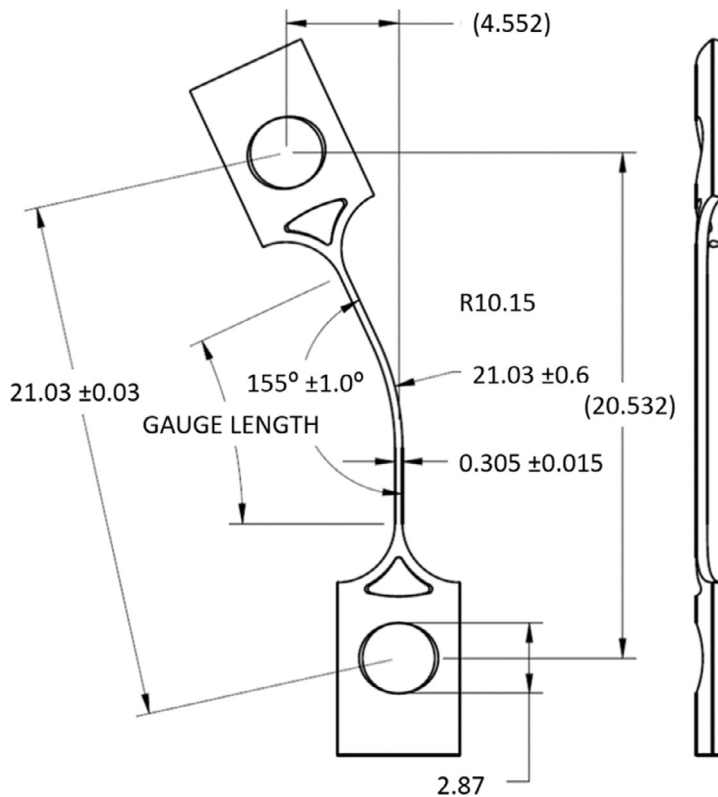


Fig. 3. Shown in mm are the critical dimensions of the final fatigue specimen after shape-setting and electropolishing. Also shown is a typical specimen in the final finished form demonstrating the uniform width and curvature at the center of the gauge section.

obtain the stress-strain curves at 37 °C for 9 ‘dogbone’ specimens laser-cut from the same tube material and having the same thermal history as the fatigue specimens. Tests were performed according to the requirements defined in ASTM F2516.²

To simulate the overstrain imposed on a medical Nitinol in an implant that is delivered percutaneously, a transient pre-straining step was carried out on each fatigue test specimen. This pre-strain was imposed by bending the specimen over a pin-gauge of diameter 2.9 mm that was pushed into a slot in a Delrin block. The bending strain achieved relative to the curved shape of the shape-set specimen was about 8.5%, and was imposed at the location where the bending strains are greatest during fatigue testing, as described below. Bending strain is defined throughout this paper by its usual meaning, namely the maximum principal strain at the outermost fibre of the gauge section during bending of the specimen, and is always the strain component parallel to the axis of the specimen. Upon removal from the Delrin block, the Nitinol fatigue test specimen returned to its shape-set configuration. As a result of such pre-straining, the outermost fibers of the fatigue test specimen were taken through an entire cycle of the hysteresis loop that converts austenite completely to martensite and then completely back to austenite. Some other fibers in the cross section near the outermost fibers also underwent the complete hysteresis loop, whereas some fibers near the center of the cross section experienced no transformation and deformed only elastically as austenite. Fibers in between the zone that deformed elastically and the region that experienced complete transformation, from austenite to martensite and back to austenite, underwent partial transformation to martensite

² ASTM F2516-18, “Standard Test Method for Tension Testing of Nickel-Titanium Superelastic Materials,” ASTM International, West Conshohocken PA (2018).

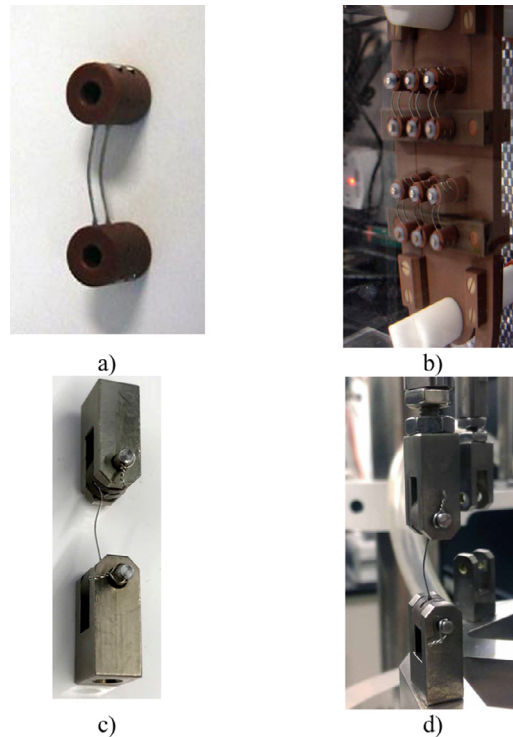


Fig. 4. a) Two fatigue test specimens (metallic coloured curved strips) held securely at each end in rollers. b) Close-up of the rotary driven fatigue testing machine showing the bracket for securing six of the units depicted in (a) and thus holding a total of twelve fatigue test specimens. The bracket has a sliding mechanism that allows extension and shortening of the fatigue test specimens. c) One specimen held in a pair of clevises that are installed between the load cell connecting rod and an arm of the multi-specimen star-shaped base plate on the TA Electroforce fatigue tester shown as shown in d).

followed by its reversal to austenite. Accordingly, all of the cross section was nominally returned to the austenite state upon release of the test specimen from the Delrin block.

Two different test systems were employed in this program. The first series of tests, series-A, was performed on a bank of custom-built rotary driven fatigue testing machines with a cam mechanism on the rotor to achieve the desired extensional and shortening displacement of the specimens tested. The bracket and setup for this test is shown in Fig. 4a and b. It can be seen that, for series-A, the specimens were tested in groups of 12, with all of them being subject to the same mean strain and strain amplitude. Each group of 12 specimens so tested is identified below by a number with the prefix A. For these series-A tests, the fatigue specimens were inserted and secured into rollers, as shown in Fig. 4a. Each roller was then fixed on a single pin on an extending bracket which was attached securely to a testing machine via a stationary shaft and the rotor having a cam that extends and shortens the specimens, as shown in Fig. 4b. During the tests, the rollers were free to rotate around the pins upon which they sat, so that no torsional constraint was imposed on them. The mean strain was achieved by choice of the distance between the centers of the rotor and the stationary shaft. The second series of tests, series-B, was performed on a group of multi-specimen electromechanical test systems (ElectroForce 3300, TA, Eden Prairie MN). In these tests, the specimens were held in a pair of clevises as shown in Fig. 4c. One clevis was attached to an arm of the star-shaped base plate at the bottom of the testing machine and the other attached to a load cell above the star-shaped plate, as shown in Fig. 4d. Each multi-specimen testing machine accommodated 6 specimens, so that series-B tests were carried out in groups of 6 specimens all subjected to the same mean strain and strain amplitude. Each group of 6 specimens so tested is identified below by a number with the prefix B. The mean strain and strain amplitude were imposed on the specimens by the oscillating vertical motion of the star-shaped base plate.

All fatigue tests were carried out with the specimens immersed in a 0.9% buffered saline solution with the temperature held to within 2 °C of 37 °C.

The bending strains imposed on the specimens were analysed by finite element computations using a superelastic constitutive law for Nitinol; the specific computations are described below. With the aid of these computations, the mean displacements and the alternating displacements were determined for each set of fatigue tests, targeting the mean strains and strain amplitudes to be implemented in each fatigue test. The setup of the series-A tests was carried out with the sliding bracket holding spare specimens that were not to be used in the campaign of fatigue tests but that were identical to those specimens utilized for the fatigue tests. The testing machine was operated with the spare specimens while adjustments were made and checked with a travelling microscope. Dial settings for the test were then fixed and the spare

specimens then in the bracket replaced by specimens to be tested for their fatigue properties. The rotary fatigue machine was operated at 3580 rpm, which is equivalent to approximately 60 Hz. Each set of test specimens was inspected optically immediately at the start of each test to ensure that the correct mean strains and strain amplitudes were being imposed, and this check was repeated periodically and the machine settings adjusted, if necessary, to maintain them. Setup of the multi-specimen electromechanical testing machines used for the series-B tests was carried out using the standard procedure specified in the instruction manual for these machines. The series-B tests were also carried out at approximately 60 Hz. The actual specimen displacements were measured and monitored throughout the test duration. The measured values for the displacements following each deformation path of test setup were used to compute the fatigue strains, *i.e.*, the mean strain and strain amplitudes for each test condition. It is therefore emphasized that the fatigue strain parameters computed for each test condition and used in the analysis of the fatigue data were based on the measured testing system displacements, and were not taken to be automatically equal to the initial target strain values that were computed to scope out choices of testing parameters.

All tests were run at a specified combination of mean strain and strain amplitude until specimens broke or had survived 400×10^6 cycles of straining. During the periodic check, any fractured specimens were identified and recorded as an interval fracture. All interval fractures were assigned a life equal to the greatest number of cycles for which the specimen was observed to be intact. Those specimens that survived to 400×10^6 cycles of straining were designated runouts. Several groups of test specimens that had all survived 400×10^6 cycles of straining without fracture were put back into the test system and the tests extended to 600×10^6 cycles of straining.

The campaign of testing was carried out with a first series, series-A consisting of 216 specimens in 18 different combinations of mean strain and strain amplitude. This number of specimens by itself meets the sample size requirements of ASTM Standard E739.³ The range of mean strain was chosen to extend from zero to 8%. After the results for these specimens were collected and assessed, additional specimens were prepared by the same processes as described above for the series-B tests, with a strategy of producing additional data points to improve the constant life model that is the objective of the research. Series-B involved 138 specimens tested in 23 combinations of mean strain and strain amplitude. The total number of specimens finally tested was 354.

4. Results for stress-strain behavior of Nitinol

To establish the elastic and superelastic constitutive parameters for the Auricchio and Taylor (1997)/Auricchio et al. (1997) constitutive model, as implemented in the Abaqus material library, a group of 9 tensile specimens was tested at 37 °C according to the requirements of ASTM Standard F2516.⁴

The characteristics of the stress-strain curves measured for the Nitinol at 37 °C are shown in Fig. 1 from a typical sample. Load-displacement data were converted to true stress-true strain curves by use of the standard definitions for true stress and true strain, namely the load divided by current cross-sectional area and the logarithm of the ratio of the current gauge length to original gauge length, respectively. However, an assumption of incompressibility was used in the process of calculating the current cross-sectional area from the current gauge length, the original gauge length and the original cross-sectional area. It can be inferred that the error in this procedure is of the order of current volume strain compared to unity. Since the volume strain, including the change in volume from austenite to martensite, is less than approximately 5%, the error in the true stress introduced by the incompressibility assumption is small. Slopes and intercepts on the resulting true stress-true strain curves were identified to define characteristic constitutive parameters, which are listed in Table 1. The elastic strain between the lower, unloading plateau of the stress-strain curve and the upper, loading plateau was approximately 0.35% for pure austenite at the left-hand end of the hysteresis loop, and approximately 0.95% for pure martensite at the right-hand end.

5. Finite element analysis of cyclic straining of fatigue test specimens

Finite element analysis (FEA) models were generated for the fatigue test specimen, as shown in Fig. 5. The Nitinol superelastic constitutive law of Auricchio and Taylor (1997) and Auricchio et al. (1997) was calibrated to the measured stress-strain behavior at 37 °C of the fatigue test specimens described in the previous section and calculations carried out quasi-statically using Abaqus-Standard (Simulia, Dassault Systèmes). The computations first imposed the cycle of straining that the specimen experienced when taken through the pre-conditioning step. Thereafter, the analysis simulated the deformation that a specimen would experience in the fatigue testing machine when held in the rollers and brackets depicted in Fig. 4b, and also as experienced by the specimen when held in the clevises in the multi-specimen testing machine, as shown in Fig. 4d. The configuration of the model, the overall mesh design and the mesh refinement are shown in Fig. 5. The boundary conditions to achieve compression of the specimen were applied as displacements of the pins inserted in rigid rollers at the centre of the hole in each end tab. The guiding rollers were free to rotate integral with the end tab without any constraining torque.

³ ASTM E739-10, "Standard Practice for Statistical Analysis of Linear or Linearized Stress-Life (*S-N*) or Strain-Life (ϵ -*N*) Fatigue Data," ASTM International, West Conshohocken PA (2015).

⁴ ASTM F2516-18, "Standard Test Method for Tension Testing of Nickel-Titanium Superelastic Materials," ASTM International, West Conshohocken PA (2018).

Table 1
Average values for stress-strain constitutive parameters for the Nitinol samples.

Stress-strain parameter	Mean value
Austenite Elastic Modulus, E_A [MPa]	71,300
Austenite Poisson's Ratio, ν_A	0.3
Martensite Elastic Modulus, E_M [MPa]	26,500
Martensite Poisson's Ratio, ν_M	0.3
Transformation Strain, ϵ^t	0.046
Clausius-Clapeyron Constant during loading, $(\partial\sigma/\partial T)_L$ [MPa/°C]	7.34
Stress at start of transformation during loading, σ_L^s [MPa]	407
Stress at end of transformation during loading, σ_L^E [MPa]	427
Reference Temperature, T_0 [°C]	37
Clausius-Clapeyron Constant during unloading, $(\partial\sigma/\partial T)_U$ [MPa/°C]	7.64
Stress at start of transformation during unloading, σ_U^s [MPa]	180
Stress at end of transformation during unloading, σ_U^E [MPa]	175
Stress at start of transformation during compression, σ_{CL}^S [MPa]	540
Volumetric transformation strain, ϵ_V^t	0.046

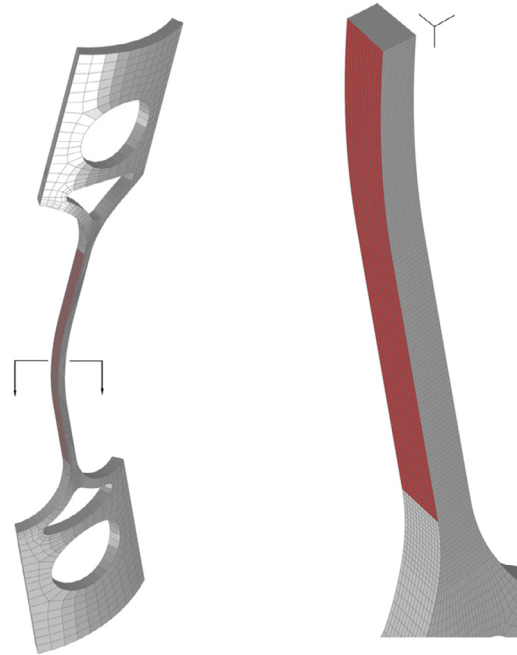


Fig. 5. Finite element mesh of the fatigue test specimen showing the mesh refinement in the gauge section and the coarse mesh in the end tab region. The element size in the gauge section across the depth, the direction in which the bending strain is linear with position, is $10\ \mu\text{m}$, *i.e.*, 32 elements to capture the strain distribution due to bending. The other element dimensions were $13\ \mu\text{m}$ along the transverse direction and $36\ \mu\text{m}$ along the longitudinal direction. Membrane elements, shown in red, are placed on the convex surface that is usually in tension during strain cycling. The membrane elements are put there to provide an accurate evaluation of the surface strain. The membrane element has negligible stiffness and strength, and therefore does not affect the mechanical behavior of the specimen. Displacement boundary conditions move the end tabs towards each other without applying any torque to the end tabs, thereby causing bending deformation of the gauge section.

Motion of one end tab of the specimen towards and away from the other causes bending and unbending of the curved gauge section, and thus generates positive principal strain, *i.e.*, extension, on one side of the gauge section, and negative principal strain, *i.e.*, shortening, on the other. Continuum solid elements of type C3D8R were used.

Refinement of the finite element model in terms of element size was carried out in a study of mesh convergence, and element sizes of $\sim 10\ \mu\text{m}$ within the gauge section were utilized for the definitive results for all subsequent fatigue specimen computations. Such an element dimension was found to be adequate in the gauge section as further reduction of size produced only small changes in the calculated strains and stresses. The final mesh used non-equiaxed element dimensions, at $10\ \mu\text{m}$ along the bending depth direction, $13\ \mu\text{m}$ along the transverse direction and $36\ \mu\text{m}$ along the longitudinal direction. As the end tab section of the specimen experienced little strain, it was assigned considerably larger elements to facilitate efficient computation. Additionally, membrane elements of type M3D4R, with a thickness of one nanometre, were applied on the tensile surface of the gauge section to achieve maximum accuracy in the computation of bending strains at the specimen surface. These elements are shown in red in Fig. 5. These membrane elements played no role in

Table 2

End tab relative displacement, u_{\min} , at minimum strain, end tab relative displacement, u_{\max} , at maximum strain, mean strain, ε_m , and strain amplitude, ε_a , for the 41 groups of specimens tested, given by group number.

Group*	u_{\min} [mm]	u_{\max} [mm]	ε_m	ε_a	Group	u_{\min} [mm]	u_{\max} [mm]	ε_m	ε_a
A03	1.230	4.000	2.88%	1.19%	B01	9.980	12.000	7.36%	0.33%
A04	-0.150	1.480	0.42%	0.59%	B02	10.640	12.000	7.47%	0.22%
A05	1.560	2.830	2.19%	0.29%	B03	8.500	10.500	7.18%	0.35%
A06	0.590	2.110	1.07%	0.51%	B04	2.520	3.940	3.85%	0.31%
A07	0.050	2.850	1.22%	1.19%	B06	2.133	4.067	3.90%	0.49%
A08	2.170	5.220	5.12%	1.07%	B08	3.405	4.805	5.24%	0.32%
A09	0.860	3.850	2.35%	1.42%	B09	3.018	4.894	5.32%	0.44%
A10	-0.360	1.880	0.39%	0.96%	B10	4.100	5.700	6.29%	0.38%
A11	0.330	1.810	0.78%	0.51%	B12	4.580	5.670	6.41%	0.25%
A12	1.690	3.680	3.21%	0.56%	B13	2.850	3.800	3.74%	0.20%
A13	0.630	2.320	1.21%	0.60%	B14	1.473	3.223	2.56%	0.47%
A14	2.880	4.550	4.78%	0.37%	B15	5.094	6.703	6.64%	0.35%
A15	0.110	2.770	1.20%	1.12%	B16	0.135	1.819	0.71%	0.59%
A16	3.910	4.700	5.22%	0.17%	B17	0.069	1.605	0.58%	0.53%
A17	5.710	6.840	6.78%	0.24%	B18	0.745	2.118	1.20%	0.41%
A18	4.540	5.450	6.28%	0.21%	B19	1.630	3.140	2.56%	0.36%
A19	4.060	5.900	6.34%	0.44%	B20	0.069	1.475	0.53%	0.47%
A20	5.080	7.110	6.63%	0.44%	B21	3.000	3.800	3.77%	0.17%
					B22	10.420	11.040	7.49%	0.10%
					B23	8.505	9.205	7.25%	0.13%
					B24	2.750	3.900	3.84%	0.24%
					B25	3.660	4.760	5.24%	0.24%
					B26	5.680	6.490	6.77%	0.18%

* See text for an explanation of the meaning of the group numbers.

the mechanical behavior of the specimen as their extremely small thickness ensured that they lack meaningful stiffness and strength.

As anticipated, when the end tabs were moved towards each other, the maximum principal strain was found to occur at the mid-point of the gauge section on the convex surface of the specimen (Fig. 6a). Similarly, the minimum principal strain occurred at the mid-point of the gauge section on the concave surface. As noted above, these principal strains are the components of strain parallel to the axis of the specimen and are bending strains at the surface of the specimen (Fig. 6b). Comparison of Fig. 6b with Fig. 6a confirms this point. The computational simulation was taken through as many as five fatigue strain cycles for each combination of mean strain and strain amplitude. The strain results in terms of mean strain and strain amplitude for each full loading-unloading reversal cycle stabilize quickly after the first full cycle. For consistency, the mean strain and strain amplitude from the third cycle were used to calculate the mean strain, ε_m , and the strain amplitude, ε_a , computed according to Eqs. (1) and (2). An example of the results for the strain amplitude is shown in Fig. 6c. It should be noted that a complete finite element analysis, including the preconditioning cycle and at least three fatigue strain cycles, was carried out for each combination of mean strain and strain amplitude. The results of the computations in terms of end tab displacements and mean strain and strain amplitude are summarized in Table 2.

6. Validation of the finite element analysis

Validation of the finite element results was carried out by comparing the computational results with experimental measurements of the load-displacement behavior of the fatigue test specimen. For this purpose, 10 fatigue specimens were tested in compression using a Model 3366 Instron testing machine (Norwood, MA). During the test, each specimen was compressed by 10 mm by moving one end tab towards the other; thereafter, the relative end displacement was reduced to zero and the specimen allowed to re-extend. Results from this test are shown in Fig. 7a for all 10 specimens. In these plots, the load applied to the specimen was normalized by EI/L^2 , where E is Young's modulus of the austenite phase as given in Table 1, $L = 21.03$ mm is the undeformed distance between the pins holding the specimen, I is the second moment of area of the specimen cross-section in the gauge length and is related to the cross-section width w , and thickness T , through $I = Tw^3/12$. The displacement, u , of one end tab towards the other is normalized by L . Fig. 7b shows the outcome of a finite element computation of the test, with the mean value of the experimental test results also plotted in that figure. At any given end displacement in Fig. 7b, the applied load representing the experimental data is the mean applied load from the 10 experimental results in Fig. 7a. In Fig. 7b, it can be seen that good agreement was achieved between the experimental and finite element results in terms of the force-displacement response.

Validation was also conducted of the local response of the specimen in its gauge length under monotonic loading and unloading. The magnitude of the bending strain in the gauge length is controlled by its curvature. Therefore, we chose to compare finite element results for the maximum gauge length curvature in the fatigue test specimen (Fig. 8a) with a measurement of the curvature obtained from a micrograph of a physically deformed specimen (Fig. 8b). In the experimental test, the specimen was compressed in a testing machine by moving one end tab towards the other by a maximum displacement

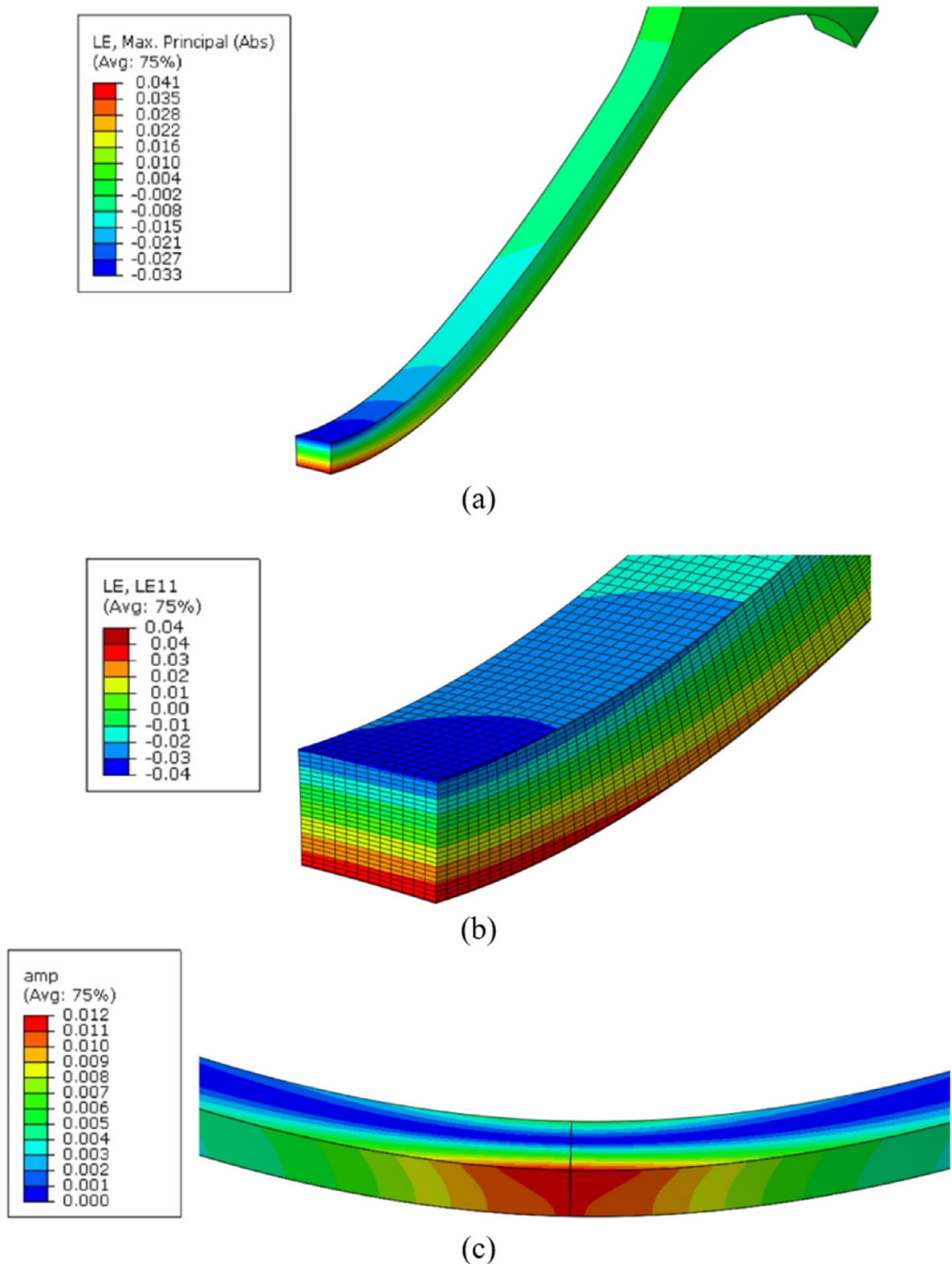


Fig. 6. (a) A colour contour plot of the maximum absolute principal logarithmic strain at the mid-point of the gauge section where the largest strain magnitude is located, with red indicating a positive principal strain and blue a negative one. (b) A colour contour plot of the bending strain component ϵ_{11} of logarithmic strain at the mid-point of the gauge section, where the x_1 -axis is parallel to the longitudinal axis of the specimen gauge section. (c) A colour contour plot of the strain amplitude computed from the third cycle of straining. The maximum strain amplitude is at the mid-point of the gauge section at the convex surface.

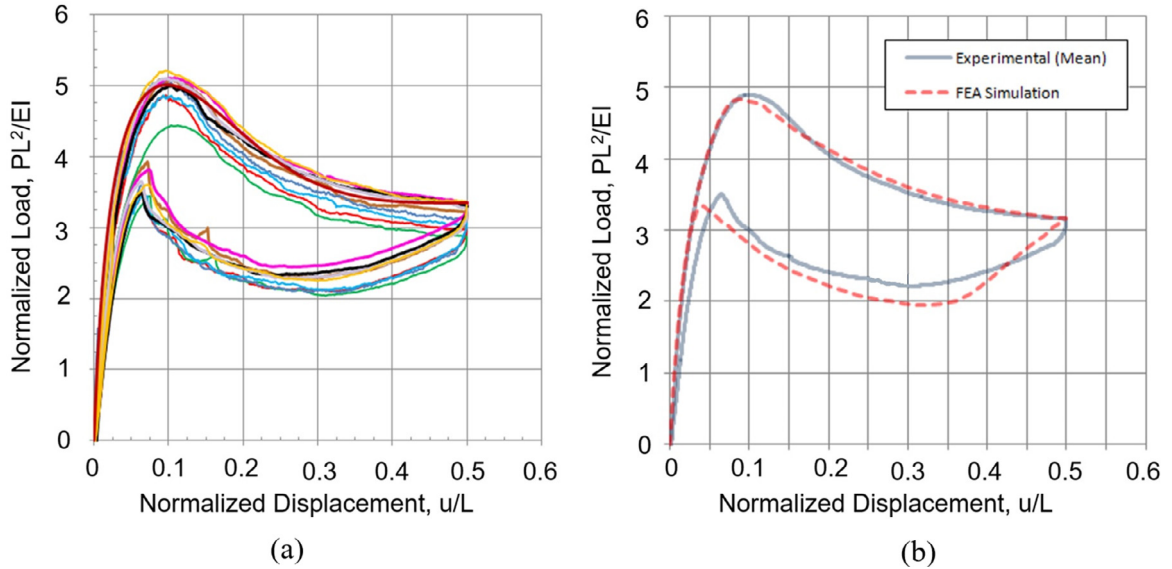


Fig. 7. (a) Load-deflection curves for compression of 10 Nitinol fatigue test specimens tested individually in an Instron testing machine. The applied load is normalized by EI/L^2 , where E is the elastic modulus of austenite, I is the second moment of area of the gauge length cross-section and L is the undeformed distance between the centers of the holes in the end tabs. The displacement, u , of one end tab toward the other is normalized by L . (b) Comparison of the finite element (FEA) simulation at a given displacement with the mean of the load results shown in (a).

of 10 mm. During this process, 10 micrographs were obtained of the curved specimen at progressively increased levels of specimen compression. The specimen was then unloaded, allowing it to re-extend and become less bent. During this process 10 micrographs were obtained at progressively diminished levels of specimen compression. The maximum curvature in the gauge length was then measured from each set of micrographs by fitting a fifth-order polynomial to the shape of its convex surface and obtaining the rate at which the tangent angle changed along the length of the gauge section. The results for maximum curvature in the gauge length are plotted in Fig. 8c as curvature versus displacement, *i.e.*, the motion of one end tab towards the other. Smooth plots were fitted to the data points of curvature versus displacement and it is these smooth plots that are shown in Fig. 8c for both loading (*i.e.*, specimen compression shown as a solid line) and unloading (*i.e.*, specimen re-extension shown as a dashed line). The relevant plots in Fig. 8c are those marked Expt (*i.e.*, experimental). A finite element simulation of the experiment was carried out and results for maximum curvature in the gauge length were obtained and treated in the same way as the experimental data. The results from the finite element simulation are also plotted in Fig. 8c for loading (full line) and unloading (dashed line) and marked FEA.

It can be seen in Fig. 8c that the finite element predictions of the maximum curvature in the gauge length agree well with the physically measured curvatures at both low and high curvatures; however, the discrepancy in the intermediate range of curvature is appreciable, suggesting that the strain analysis is more reliable in both the low and high strain range, and less reliable in the intermediate strain range. Note that the curvature predicted by finite element analysis is less than the experimental curvature in this intermediate range, suggesting that the finite element analysis underestimates some measures of strain in this intermediate range. This point will be further explored below in the Discussion section.

7. Results of the fatigue tests

Fatigue life data from the initial campaign of tests, series-A, are presented in Fig. 9a in the form of a Goodman diagram, where results for all 216 specimens are shown in terms of strain amplitude versus mean strain with a symbol indicating their fracture status. Specimens fractured before reaching 400×10^6 cycles are represented by a cross; specimens reaching 400×10^6 cycles without fracture are referred to as runouts and represented by open circle symbols. If there is only an open circle, all 12 specimens in the group tested at the relevant mean strain and strain amplitude were runouts. If there is only a cross, all 12 specimens in the group tested at the relevant mean strain and strain amplitude fractured before 400×10^6 cycles. If there is a cross and a circle some of the 12 specimens tested at the relevant mean strain and strain amplitude were runouts and some fractured before 400×10^6 cycles. Some specimens fractured prior to 10×10^6 cycles. Combinations of strain amplitude and mean strain for which this happened are marked by a diamond symbol in addition to a cross, indicating that some or all of the specimens tested fractured prior to 10×10^6 cycles.

Similarly, fatigue life data from the second campaign of tests, Series-B, are presented in Fig. 9b with the same symbolism as used for Fig. 9a. However, Series-B was carried out in groups of 6 specimens tested at the same mean strain and strain amplitude. Thus, a cross alone means that all 6 specimens in the group fractured before 400×10^6 cycles, an open circle

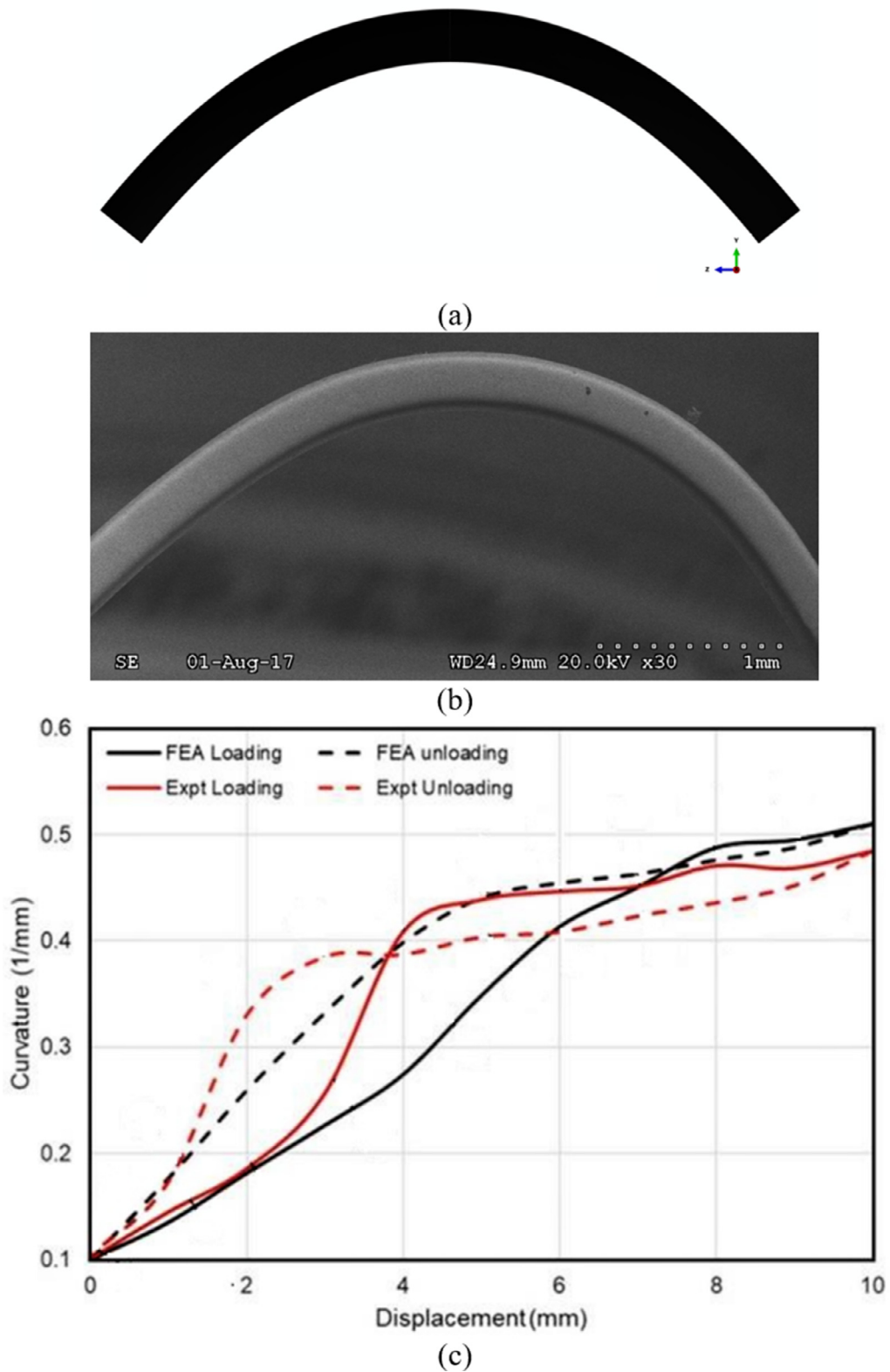
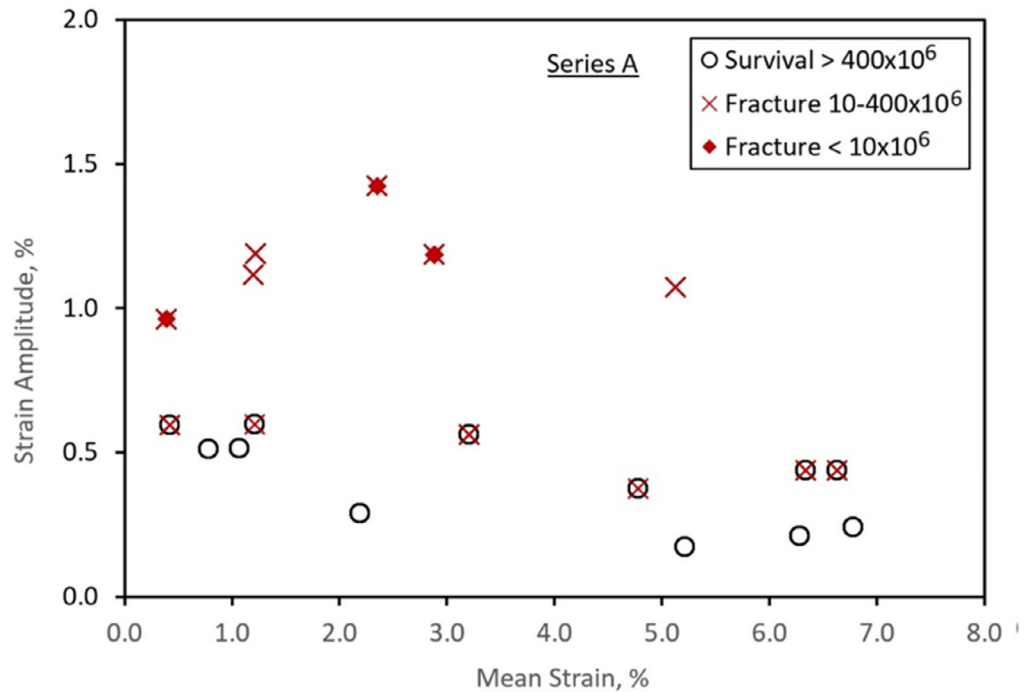
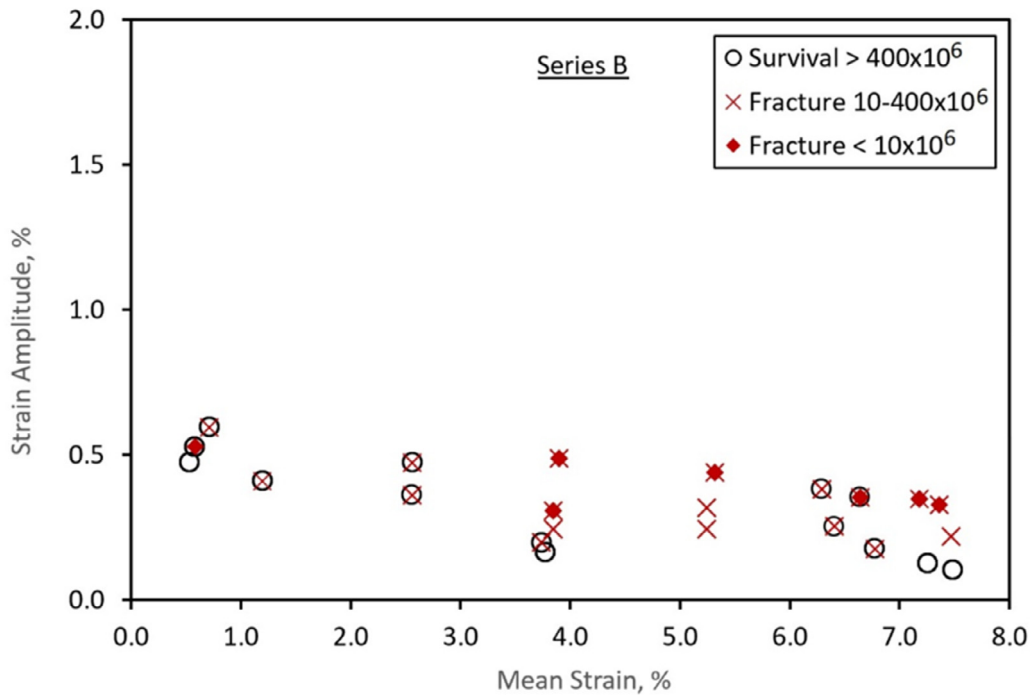


Fig. 8. (a) An example of a finite element model in the deformed configuration used to compute the maximum curvature in the gauge section. (b) An example of a micrograph of a bent fatigue test specimen used for measurement of the maximum curvature in the gauge length. (c) Plot of the maximum curvature in the gauge length versus displacement of one end tab towards the other, for both loading and unloading. Results are shown for both experimental measurements (Expt) from micrographs such as that shown in (b) and finite element computations (FEA) obtained from model results such as that shown in (a).



(a)



(b)

Fig. 9. Goodman-Haigh diagrams of the strain amplitude versus the mean strain for the campaigns of fatigue tests showing the status of specimens after 400×10^6 cycles of straining for (a) the Series-A campaign; and (b) the Series-B campaign. In (a) & (b) the crosses represent specimens that fractured after 10×10^6 cycles of straining but before 400×10^6 cycles. The open circles represent runout specimens that survived without fracture at 400×10^6 cycles. The solid diamonds represent specimens that fractured before 10×10^6 cycles. Collocated symbols indicate that the group contained some specimens that experienced the indicated outcomes.

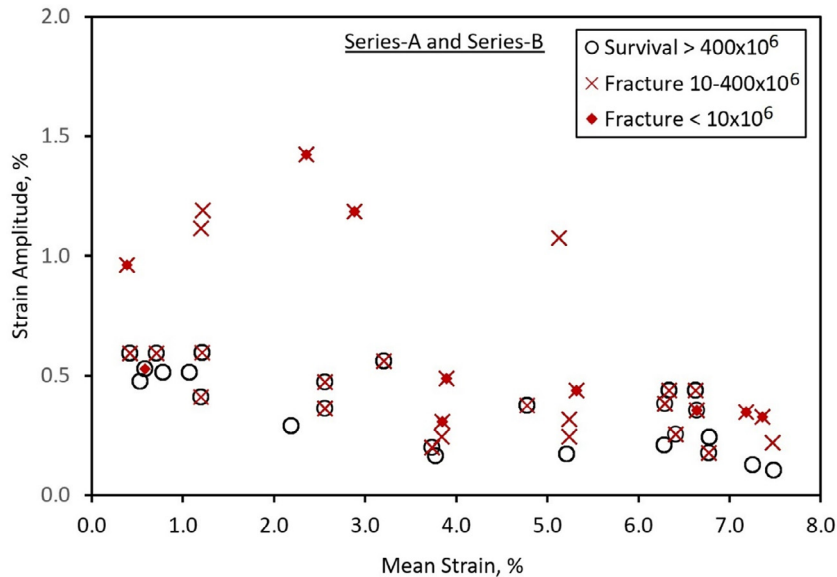


Fig. 10. Goodman-Haigh diagram of the strain amplitude versus mean strain for the entire campaign of fatigue tests showing the fracture status of test specimens after 400×10^6 cycles of straining. The crosses represent specimens that fractured after 10×10^6 cycles of straining but before 400×10^6 cycles. The open circles represent runout specimens that survived without fracture at 400×10^6 cycles. The solid diamonds represent specimens that fractured before 10×10^6 cycles. Multiple symbols plotted together indicate that the relevant group contained some specimens that experienced the indicated outcomes.

alone indicates that all 6 specimens were runouts, and a cross and an open circle together indicates a mixture of fractures and runouts within the 6 specimens involved.⁵ A diamond and a cross together indicate that the group of 6 had some specimens that fractured prior to 10×10^6 cycles. In Fig. 9b it can be seen that there are 2 groups of specimens in which 1 or more specimens fractured prior to 10×10^6 cycles with the balance of the group being runouts. In addition, there is 1 group that had some specimens fracture prior to 10×10^6 cycles, some that fractured between 10×10^6 and 400×10^6 cycles and some that were runouts.

The results of both campaigns, from Fig. 9, are combined and plotted in Fig. 10 again in the form of a Goodman diagram, with the same symbolism used as in Fig. 9. Careful examination of Fig. 10 to estimate where a dividing line can be drawn between fracture at 400×10^6 cycles and survival at 400×10^6 cycles, based mainly on the location of the crosses and the circles, suggests that higher mean strains require smaller strain amplitudes to prevent fracture prior to 400×10^6 cycles of bending, but with a break in the slope of the dividing line at around 3% mean strain. Thus, a preliminary assessment of these results indicates that the constant life model for the data at 400×10^6 cycles is monotonic, but also that it does not conform to the common straight-line Goodman diagram of strain amplitude versus mean strain that usually prevails for metals with elastic-plastic constitutive behavior.

However, a more thorough investigation of this question using statistical analysis is described below; this analysis is based on the data that determine how many cycles a given specimen survived, not just on whether it did, or did not, survive to 400×10^6 loading cycles.

8. Statistical analysis of constant life model

Given the data in Fig. 10, we assume that the constant life model at 400×10^6 cycles can be represented by two linear segments with the dividing line around 3% mean strain. We do not prejudice the location of these two straight lines, but determine them according to a maximum likelihood procedure coupled to estimates of confidence intervals that give one-way conservative limits on the effective fatigue strain amplitudes that are then used as the final model. In addition, we make assumptions regarding the statistical distribution of the fatigue life, N (i.e., number of strain cycles at failure), for the Nitinol, based on considerations that are known to be satisfactory for most metals (Harlow et al., 2016; Schmidt et al., 2019); indeed, there is evidence that these assumptions are also suitable for the Nitinol under consideration (Robertson et al., 2012). Specifically, we assume that the fatigue life distribution for a sufficiently large sample under identical fatigue strain conditions can be described by a two-parameter Weibull (1961) distribution. Furthermore, the Weibull distribution shape parameter, β (see Appendix A), is assumed to remain constant for varying strain amplitude conditions for each mean strain

⁵ It should be noted that 5 groups of Series-B specimens were re-tested after having survived 400×10^6 cycles without fracture and were continued to 600×10^6 cycles. A majority of these re-tested specimens also survived without fracture to 600×10^6 cycles. One third of these specimens had fractures between 400×10^6 and 600×10^6 cycles.

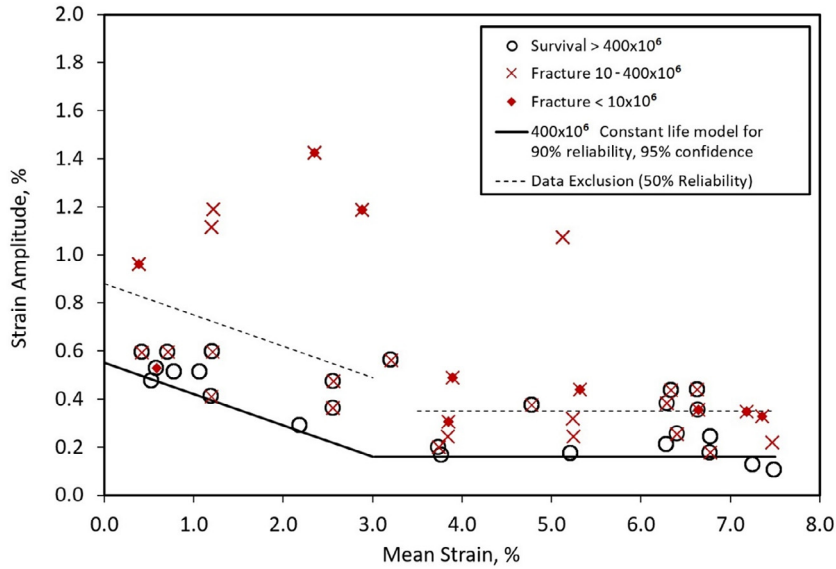


Fig. 11. Fracture diagram and constant life model for a life of 400×10^6 cycles of straining. The crosses represent specimens that fractured after 10×10^6 cycles of straining but before 400×10^6 cycles. The open circles represent runout specimens that survived without fracture at 400×10^6 cycles. The solid diamonds represent specimens that fractured before 10×10^6 cycles. Multiple symbols plotted together indicate that the relevant group contained some specimens that experienced the indicated outcomes. The dashed lines are the constant life model deduced statistically at 400×10^6 cycles of straining with 50% reliability and 95% confidence from a preliminary analysis. The solid lines are the constant life model deduced statistically at 400×10^6 cycles of straining with 90% reliability and 95% confidence based on the final analysis but excluding data that lies above the 50% reliability constant life diagram.

regime, but the scale parameter is assumed to obey an inverse power-law relation as a function of the effective fatigue strain amplitude (Harlow et al., 2016; Schmidt et al., 2019). For this purpose, we introduce a parameter K that is related to the scale parameter in the inverse-power law relationship for fatigue life under a given combination of mean strain and strain amplitude. These assumptions are summarized and illustrated in Appendix A, which describes the development of the statistical constant life model.

Since we assume that the constant life model consists of straight lines, we proceed with an effective fatigue strain amplitude, ε_e , that is a combination of the strain amplitude and the mean strain, as follows:

$$\varepsilon_e = \varepsilon_a + \xi \varepsilon_m \tag{4}$$

where ξ is a parameter governing the impact of mean strain on fatigue life. For the model at mean strains higher than 3% we set $\xi = 0$. We note that the effective fatigue strain amplitude defined in Eq. (4) is the equivalent of the Stulen (1965) effective stress model recommended for fatigue in the military design handbook,⁶ and found to apply to common alloys. As noted above, we also invoke the Basquin (1910) or Coffin-Manson (Coffin, 1954) inverse-power-law life model for stress-life plots in fatigue, but converted to a strain-life model, such that, at any given percentage of survival, the fatigue life would be inversely proportional to the effective fatigue strain amplitude raised to a power n . The resulting form of the 2-parameter Weibull (1961) distribution that we utilize is given in Eq. (A1) in Appendix A.

As described in Appendix A, the values of the parameters K , ξ , n and β for the model at mean strains less than 3% are obtained by the maximum likelihood method (Meyer, 1965; Nelson, 1990; Meeker and Escobar, 1998) for N strain cycles at failure at a specified reliability ρ , where ρ is the fraction of samples surviving to N cycles. The values of the parameters K , n and β at mean strains higher than 3% are obtained by an identical procedure. To obtain a fatigue reliability model at a specified confidence level on the effective fatigue strain amplitude, the likelihood ratio interval method (Nelson, 1990; Meeker and Escobar, 1998) is used. The computations were performed with use of Mathcad (Version 15). Accordingly, we obtained the results for a life of 400×10^6 cycles of straining, and designate the resulting value of ξ to be ξ^* (with $\xi^* = 0$ at mean strains higher than 3%). We then compute the value of the effective fatigue strain amplitude, $\bar{\varepsilon}_e$, associated with 90% reliability at 95% confidence for 400×10^6 cycles to failure, with one value for mean strains below 3% and a different one for mean strains above 3%.

The results from Eq. (4) with $\xi = \xi^*$ and $\varepsilon_e = \bar{\varepsilon}_e$ are then plotted in Fig. 11 as dark black lines representing the constant life model for the fatigue of Nitinol at 400×10^6 cycles of straining with 90% reliability at 95% confidence on the effective fatigue strain amplitude. The intercept of this line at zero mean strain is at a strain amplitude of $\varepsilon_a = \bar{\varepsilon}_e = 0.55\%$, thus giving the strain amplitude lower bound for a life of 400×10^6 cycles at an R -ratio of -1 . The value of $\xi = \xi^*$ is 0.13 for mean strains less than or equal to 3%, so that the strain amplitude lower bound is 0.16% for a 400×10^6 cycle life at a

⁶ Metallic Materials and Elements for Aerospace Vehicle Structures, MIL-HDBK-5E, Vol. 1 (1987).

mean strain of 3%. Above a mean strain of 3%, the strain amplitude lower bound is $\varepsilon_a = \bar{\varepsilon}_e = 0.16\%$ for a life of 400×10^6 cycles, independent of mean strain.

In Fig. 11, the dashed lines represent the 50% reliability boundary obtained in a preliminary analysis. For easy reference, the fracture status of all tested specimens is superimposed on the constant life diagram (Fig. 11) using the same symbolism as utilized for Figs. 9 and 10; i.e., solid diamonds represent specimens that fractured at, or before, 10×10^6 cycles, crosses represent fractures between 10×10^6 and 400×10^6 cycles, and circles represent runouts beyond 400×10^6 cycles, including some groups that survived beyond 600×10^6 cycles of straining. As above, collocated overlapping symbols indicate that there were some specimens at the relevant mean strain and strain amplitude in each of the categories represented.

9. Discussion

We observe that our constant life model at 400×10^6 strain cycles for medical grade Nitinol alloy, shown in Fig. 11, is monotonic, in contrast to other results reported in the literature by Robertson et al. (2012). Our model does have an unusual feature for a metal that it consists of two segments: one, for $0 \leq \varepsilon_m \leq 3\%$, where the strain amplitude, to keep the life constant at 400×10^6 cycles, has to fall as the mean strain is increased, and the other, for $3\% < \varepsilon_m < 8\%$, where the required strain amplitude for constant life is independent of the mean strain. Furthermore, we offer no insights on the features of the constant life diagram at mean strains above 8% as we did not test for such conditions.

Of significance is that there are important consequences given the shape of the constant life diagram. One is that, for a life of 400×10^6 cycles, the allowable strain amplitude at a mean strain above 3% is significantly less than the allowable strain amplitude at zero mean strain. Our results in Fig. 11 indicate that at zero mean strain a strain amplitude of 0.55% is consistent with 400×10^6 cycles of strain, at 90% reliability with 95% confidence, whereas at mean strains above 3% the allowable strain amplitude for the same life is 0.16%. This is of considerable significance as medical implants made of Nitinol are often operated at nonzero mean bending strains, with the implication that the safe allowable strain amplitude for a life of 400×10^6 cycles of straining may be as low as 0.16%. Since the inverse-power-law for the strain-life behavior, at long lives such as 400×10^6 cycles, is quite insensitive to the number of cycles to failure, the inference for lives somewhat shorter than 400×10^6 cycles of straining is similar. Thus, for lives as low as 100×10^6 cycles, the allowables, in terms of strain amplitudes at a given mean strain, will be quite similar to those depicted by our constant life model for 400×10^6 cycles of straining. We note, however, that the results in Fig. 11 that identify fractures at 10×10^6 cycles or less suggest that fatigue life data obtained for Nitinol using protocols that define a runout to occur at 10×10^6 cycles will be a poor predictor of fatigue lives that demand 100×10^6 cycles or 400×10^6 cycles. The reason is the significant number of specimens in the data set displayed in Fig. 11 that survive 10×10^6 cycles but fail before 400×10^6 cycles. Those cases of most concern are those that exhibit this behavior at relatively low strain amplitudes.

A corollary of one of our conclusions is that one cannot rely on strain-life data obtained at zero mean strain to deduce the fatigue life for Nitinol at nonzero mean strains. Based on the constant life models often identified in the literature (Robertson et al., 2012), it is usually assumed that the fatigue life of Nitinol is insensitive to the mean strain, or even that the fatigue life improves as the mean strain is increased. Our data shown in Fig. 11, and the associated constant life model that we have inferred from them, contradict these notions and calls into question the validity of such a claim.

That our constant life model for Nitinol at 400×10^6 strain cycles is very different from many already in the literature for cycles to failure approaching 10×10^6 cycles requires some consideration. There are several reasons why the results of others may be different from ours. One is that 10×10^6 cycles of straining is an inadequate test for Nitinol that must survive as a medical implant for 400×10^6 heart beats in 10 years in the cardiovascular system, or for 100×10^6 cycles of breathing in 10 years, as is the case with inferior vena cava filters. As noted above, it is clear from our results that Nitinol fatigue data obtained for 10×10^6 cycles of straining cannot be used to extrapolate to lives of 400×10^6 cycles or even to 100×10^6 cycles. Thus, an important conclusion is that, simply put, previous fatigue tests of medical implant grade Nitinol were too short in regard to the number of cycles of straining that were undertaken.

Another reason for the differences between previously published fatigue data for medical implant grade Nitinol and our results in the current paper is that in several cases of data published by others there was no pre-straining to an overstrain prior to implementation of the fatigue tests (Tabanlı et al., 1999, 2001; Morgan et al., 2003). As the effect of such overstraining is to convert the most highly strained regions of the material in the specimen fully to martensite and then, upon relaxation of the overstrain, to allow the martensite to convert back to austenite, overstraining effectively produces a material that is different from that which prevails prior to overstraining. The reason for this is that the microstructure and the texture of the material, even after it returns to austenite, is usually modified in the process of overstraining and relaxation (Robertson et al., 2012). Thus, prior overstraining of Nitinol before fatigue cycling is of great significance as it determines the material for which fatigue data are collected, and fatigue data from tests without prior overstraining cannot be used to gauge the potential fatigue life of a Nitinol that is subjected to overstraining. As medical implants made from Nitinol are almost all overstrained during percutaneous implantation (Duerig et al., 1999; Stöckel et al., 2004; Grassi, 1991; Lanz et al., 2019), it is of critical importance that *in vitro* fatigue data for them be obtained on specimens that have been subjected, as ours were, to the appropriate degree of prior overstraining. Thus, we conclude that an explanation for some of the differences between our fatigue data in the current paper and some of the data in previously published papers is the lack of prior overstraining in the previous work by Tabanlı et al. (1999, 2001) and Morgan et al. (2003), and perhaps of others.

Another reason why the results of others may differ from our own is that much of the data in the literature is interpreted through finite element analysis of deformations of complex-shaped specimens, with a constitutive model for Nitinol that is fitted to its stress-strain curve. This leaves open the possibility that errors arise in the computations of the strains that are present in the critical regions of the specimens, whether through incomplete aspects of the constitutive law, or through inadequate accuracy in the finite element results. Our experience with medical implants, such as prosthetic heart valves and stents that have features in them very similar to those in the diamond strut specimens often used in fatigue testing of medical implant grade Nitinol (Robertson et al., 2012), suggests that the strains in critical locations are very sensitive to device geometry, so that, as pointed out by Tripathy et al. (2019), peak strains can vary considerably from specimen to specimen even when within dimensional tolerance. Thus, a finite element analysis may be quite misleading as to the strains that are actually occurring in a tested specimen. Consequently, the interpretation of fatigue data from specimens with a complex shape, such as the diamond strut specimen used by Tolomeo et al. (2000) and Pelton et al. (2003), is likely to be quite inaccurate. We believe that this source of error is a contributor to some of the differences between some fatigue data previously published for medical implant grade Nitinol and our data in the current paper.

Another point is that even if the finite element results are accurate, the question arises of how to convert them to fatigue strain magnitudes in the critical areas of the specimens. If the mean strain and strain amplitude in the studies of others were not analysed properly, errors in the magnitudes of the relevant strains could have been made when the fatigue specimen was calibrated. For example, if the strain cycling associated with each loading and unloading of the specimen is omitted from the computation, and finite element analysis carried out only for monotonically increasing deformation of the specimen, then the strain amplitude and the mean strain in the critical region of the specimen will be erroneously recorded. A detailed discussion on the proper computation of the strain amplitude and mean strain for Nitinol fatigue has been provided in a previous study by Tripathy et al. (2019). For example, it is of critical importance that if numerical results are to be used to calibrate the cyclic and mean strains occurring in a fatigue test of a specimen, they should be obtained in the following manner. First, a cycle of overstraining should be simulated to pre-condition the finite element model and its constitutive law so that subsequent numerical results are obtained with the finite element model and the constitutive law in the correct condition for predicting the behavior of the fatigue specimen when it undergoes the fatigue straining. Then, to obtain the correct strain amplitude and mean strain that the material experiences at each location within the specimen, the finite element model must be taken to the appropriate level of deformation of the specimen and then put through enough cycles of deformation for a steady-state response to be achieved so that an accurate strain amplitude and an accurate mean strain can be computed for the critical region of the specimen. There is no shortcut to this procedure and approaches that do not carry out the full simulation will give inaccurate predictions of the strain amplitude and mean strain in the critical region of the specimen. We are convinced that errors will be introduced by failure to follow the full procedure which we have just described, and that such errors in previous work may have contributed to some of the differences that we see between the fatigue data for medical implant grade Nitinol in that previous work and our data in the current paper. To illustrate this point, in Appendix B we have computed and plotted our data using an erroneous approach for utilizing finite element analyses of our fatigue test specimens; as an outcome of that erroneous approach we obtain a diagram of strain amplitude versus mean strain that would support a non-monotonic model for constant life at both 10×10^6 cycles to failure and at 400×10^6 cycles to failure (see Fig. B2). In the light of Fig. 11, such a non-monotonic constant life model is clearly wrong. As well as describing the erroneous methodology for calibrating a fatigue test specimen, Appendix B also gives further details of how the correct approach is carried out.

We are aware that our results for strain have been obtained through a process in which finite element results have been carried out based on a Nitinol constitutive law that was calibrated to measured stress-strain curves. However, we make two comments here. The first is that our specimen, as depicted in Fig. 3, is of a relatively simple shape and, compared to the more complex ones often used for data in the literature (see Robertson et al., 2012), is thus less likely to lead to significant errors in computation and constitutive behavior. Specifically, the strain magnitudes will vary only slightly from specimen to specimen for samples all within dimensional tolerance. Second, we have been careful to validate our results, with the outcome of that process given in Figs. 7 and 8. We have detected some discrepancies in the prediction of curvature between our finite element analysis and the measurements on tested specimens, which is likely due to the localized stress-induced austenite-martensite transformation and its reversal as reported by Mao et al. (2008) and Jiang et al. (2017). Localized stress-induced phase transformation was not modeled in our finite element analysis. However, we note that these discrepancies have little effect on the calculations that led to our constant life model depicted in Fig. 11. We feel confident in claiming this because it is our deduction that the discrepancies will mainly affect the prediction of mean strain but have little effect on the predictions of strain amplitude, because the strain amplitudes throughout that permit a 400×10^6 cycle life are largely within the incrementally linear elastic regime. Furthermore, the only computations that may have affected the calculations that led to the constant life model in Fig. 11 are those that have mean displacements in Fig. 8 greater than 2 mm but less than 6 mm. Since the fatigue results are insensitive to mean strain at values greater than 3%, we identify only computations for a mean displacement greater than 2 mm but leading to a mean strain less than 3% as having possibly affected the computation of the constant life model. Out of the 41 groups of specimens tested, we find that only 5 groups fall into this category. Thus, we feel confident that our estimates of strain in the critical region of our specimen are reliable in almost all of the cases that can have an impact on computation of the constant life model depicted in Fig. 11.

To support this inference, we have attempted a more specific validation by measuring the strain directly using digital image correlation during compression of the specimen and comparing that with the equivalent results from the finite ele-

ment analysis. Without going into the details of how the strain measurements were made, we show the results in Fig. 12. It can be seen that there is excellent agreement between the finite element analysis and the measured strains up to about 3% strain. However, there is a discrepancy of up to 2% in the range of strains from 3% to 7%. While this is notable and deserving of further investigation, we observe that the discrepancy does not cause us to reconsider our constant life diagram for the reasons as follows. We note that in Fig. 11, one segment of the constant life model prevails for mean bending strains up to 3%, which is also the regime where the validation provided by Fig. 12 proves to be accurate. Therefore, we regard the constant life model in the segment of the diagram in Fig. 11 for $0 \leq \varepsilon_m \leq 3\%$ to be robust. For mean bending strains above 3% in Fig. 11, there may be an adjustment called for by the increase in the strain magnitudes involved; however, the fact that the constant life model in this region is horizontal, means that any required adjustment is actually moot. This point is reinforced by the fact that the strain amplitudes, near those associated with the constant life model for mean strains above 3%, at around 0.16%, are quite small and within the incremental range of elastic response within the hysteresis loops. It is noted above that the limits on linear elastic response within the hysteresis loop of the material ranges from 0.35% to 0.95%. Therefore, it is quite certain that the strain amplitudes computed for the results in Fig. 11, close to those associated with the constant life model for mean strains above 3%, are quite accurate, even if the mean strains themselves need upward adjustment. Thus, we conclude that our constant life model is robust over the whole range of mean strains that we consider.

The Weibull (1961) statistical analysis presented in the section above, and in detail in Appendix A, relies on the basic concept of the strain-life relationship invoked as part of the inverse-power-Weibull-life-stress-distribution model (Eq. (A1)) (Shanmugam et al., 2019). To appreciate the fracture life distribution, it is instructive to plot the strain amplitude-life ($S-N$) relationship using the effective fatigue strain amplitude for mean strains less than 3% and the strain amplitude for mean strains greater than 3% versus the number of cycles to fracture, both shown in Fig. 13. For these plots the parametric values listed in Table A1 are used in conjunction with Eq. (A17), and we consider them to give a lower bound on the effective fatigue strain amplitude, ε_e as a function of the life, N . It can be seen that the results in Fig. 13 demonstrate that the statistical model for 90% reliability captures the large majority of the fractured specimens, with only 5 of them exhibiting failure while lying below the line representing the lower bound fatigue limit curve for 90% reliability at 95% confidence from the statistical analysis. As 354 specimens were tested, this point is self-evident.

Furthermore, it can be seen that the lower-bound fatigue limit curve for 90% reliability at 95% confidence from the statistical analysis, shown in Fig. 13, continues to decline in terms of strain at lives greater than 10×10^6 cycles. Therefore, a sample of specimens divided into those that fractured before 10×10^6 cycles and those that are defined to be runouts at 10×10^6 cycles, as is often the case in fatigue testing of Nitinol, is unlikely to lead to an accurate prediction of the allowable strain for a safe fatigue life of 400×10^6 cycles, or even of 100×10^6 cycles. Indeed, an approach that limits itself to testing to 10×10^6 cycles is clearly non-conservative. At this point, it should be noted that the so-called 0.4% fatigue strain limit for 10×10^6 cycles independent of mean strain proposed by Pelton et al. (2008) is not based on any statistical analysis, but rather on visual inspection of the plots of the raw fracture data. This is clearly inadequate as the lower bound fracture data points will tend to change as the number of test specimen increases.

A fractography study was undertaken for representative specimens to confirm the fatigue initiation location and origin. Specimens fractured under fatigue usually experienced initiation near the plane within the gauge section where maximum cyclic bending fatigue strain is experienced. A typical fracture surface examined under a scanning electron microscope is shown as Fig. 14. The vast majority of the fractured specimens indicated the presence of an inclusion at the crack initiation site (Fig. 14c), although some specimens showed no such apparent inclusion or defect causing the initiation of the fracture (Fig. 14d). As expected, fatigue crack initiation occurred on the tensile face of the bending specimen (Fig. 14a), except for several groups of specimens where the R -ratio was low or negative and where fractures initiated from the compressive side (Fig. 14b). This may be due to the tensile residual stress and compressive damage caused during the pre-conditioning cycle prior to fatigue testing. Such effects of a compressive pre-conditioning strain have been reported previously by Gupta et al. (2015) and Senthilnathan et al. (2019). As its mechanistic effect is still uncertain, this is certainly deserving of further study.

We appreciate that there is a limitation of our constant life strain limit model in Fig. 11 as it is based on the specific set of experimental data described in this paper for a specific Nitinol composition and heat treatment. Specific details of the fatigue behavior of Nitinol can be expected to depend on variations of chemical composition, heat treatment process, surface condition and preconditioning history experienced by the device. However, as all medical implant grade Nitinols are similar in composition and tend to receive similar heat treatments, we expect the general trends revealed in our constant life diagram and strain-life graph to have broad applicability. Our approach to determining fatigue resistance for medical implant grade Nitinol should serve as a paradigm for the evaluation of any specific Nitinol in the context of the device design it is intended for. Most importantly, our work indicates that careful study of the effect of mean strain on the fatigue life of medical implant grade Nitinol is essential, and thus future work should focus attention on the mean strain range within which the intended design will operate in order to achieve the highest precision in its life prediction. In addition, we have not sought to define the precise law governing the fatigue life of Nitinol, but instead focused, for component design purposes, on obtaining a conservative estimate at 95% confidence for lower bound values on the effective fatigue strain amplitude for 90% reliability at a fatigue life of 400×10^6 cycles.

Furthermore, the exact location of the dividing line between the fatigue behavior at low versus high mean strain may be subject to change depending on future testing that produces further data. However, the implication regarding the design

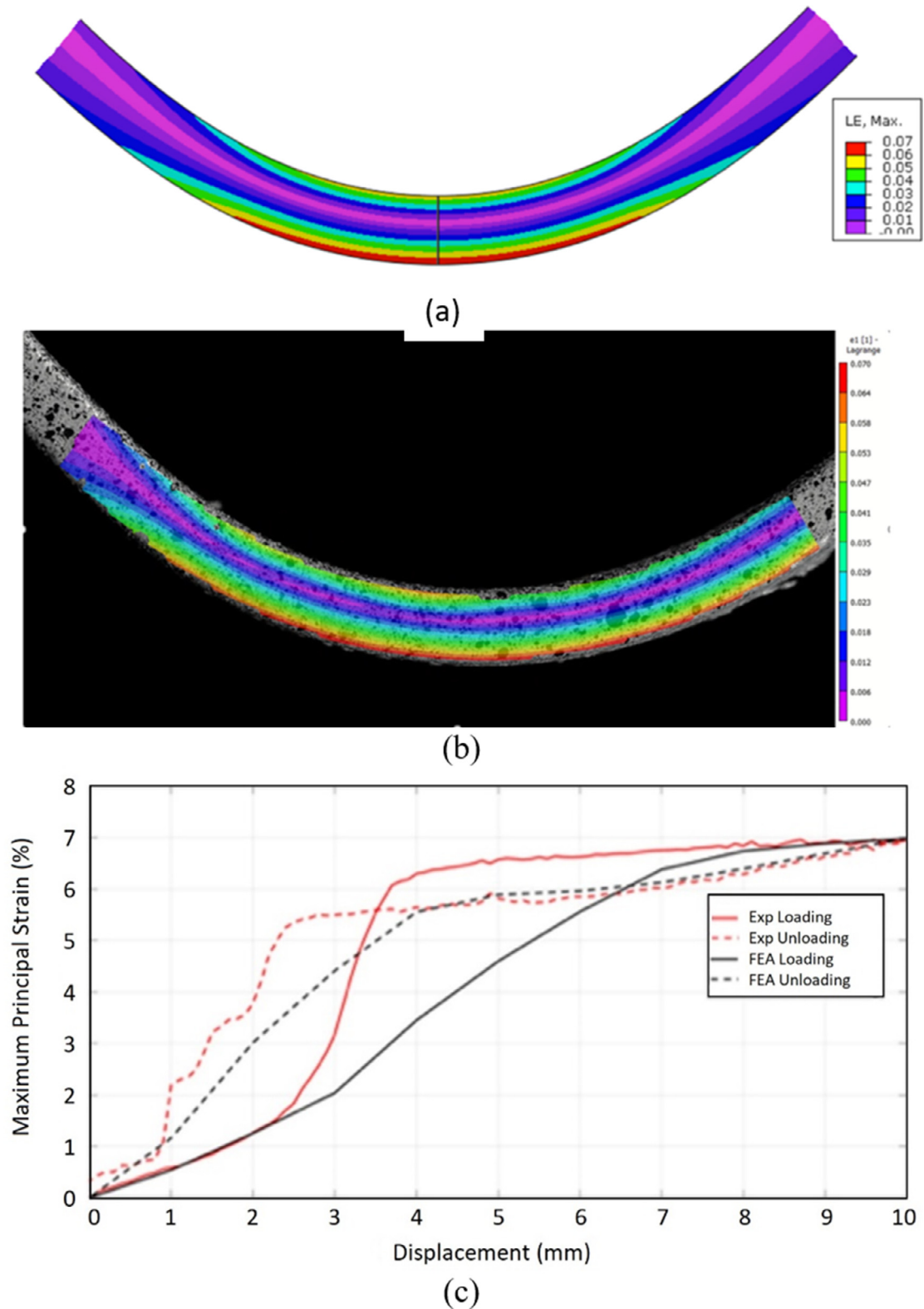


Fig. 12. Comparison of direct measurements of strain in the fatigue test specimens with equivalent computations by finite element analysis. a) Contour plot of maximum principal logarithmic strain at 10 mm relative end tab displacement from the finite element analysis. b) Contour plot of maximum principal strain at 10 mm relative end tab displacement for a typical fatigue specimen. The results are obtained by digital image correlation. c) The maximum values of the maximum principal strain in the specimen are plotted against the displacement of one end of the specimen towards the other. Results from both digital image correlation (Exp) and finite element analysis (FEA) are shown during both loading and unloading.

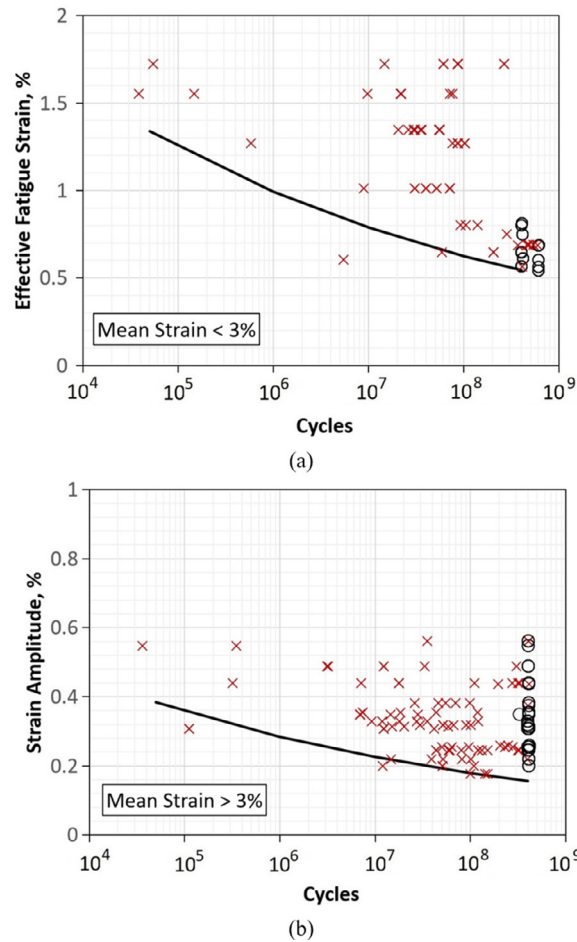


Fig. 13. Strain-life plots of effective fatigue strain amplitude versus the number of cycles to fracture. If a specimen survived 400×10^6 cycles, it was identified as a runout and the data for it plotted at 400×10^6 cycles as open symbols. The cross symbols indicate fractured specimens. The black line is a lower bound fatigue limit curve for a 90% reliability and 95% confidence from the statistical analysis. (a) The effective fatigue strain amplitude is computed from Eq. (4) using the mean strain and the strain amplitude for each group tabulated in Table 2 with $\xi = 0.13$ when the mean strain is less than 3%, and (b) The effective fatigue strain amplitude is equal to strain amplitude with $\xi = 0$ when the mean strain exceeds 3%.

of Nitinol-based devices in general is clear. Devices that experience greater than 2% mean strain will have a much lower tolerance to strain amplitude than the 0.4% allowable proposed by Pelton et al. (2008). Thus, without rigorous fatigue testing at nonzero mean strains of a given Nitinol alloy, reliance on proposals, such as that made by Pelton et al. (2008), that increases in the mean strain can increase, or at least have little negative effect, on lifetimes, there is a danger of premature fatigue fracture in a specific Nitinol device that is subject to fatigue loading if mean strains exceed approximately 1%.

The large spread in the fatigue lifetime distribution for specimens tested under identical effective fatigue strain conditions also deserves more attention. Some tests suggest that some specimens may survive more than 400×10^6 cycles of straining while others fracture under tens of millions of cycles under identical test conditions. This is consistent with the usual observation that metal fatigue is controlled by a weakest-link statistical phenomenon while the presence of non-metallic inclusions may be the culprit for fatigue initiation. High purity Nitinol material with reduced inclusion size and volume fraction, as well as surface finish minimizing the presence of process-related surface imperfections, should be explored further to improve the fatigue resistance of this important implant alloy.

10. Conclusions

We have carried out bending fatigue tests of an electropolished medical grade Nitinol to 400×10^6 cycles of straining at 37 °C. We find that, for a reliability of 90% with 95% confidence, the strain amplitude lower bound is 0.55% at zero mean strain to achieve a lifetime of 400×10^6 cycles of straining, whereas the strain amplitude lower bound for the same life is 0.16% at a mean strain of 3% or greater. Between a mean bending strain of 3% and one of 8%, for a reliability of 90% with 95% confidence, the strain amplitude lower bound to achieve a lifetime of 400×10^6 cycles of straining is insensitive to the mean strain and is 0.16% in this regime. The constant life model, for a lifetime of 400×10^6 cycles of straining, in terms of

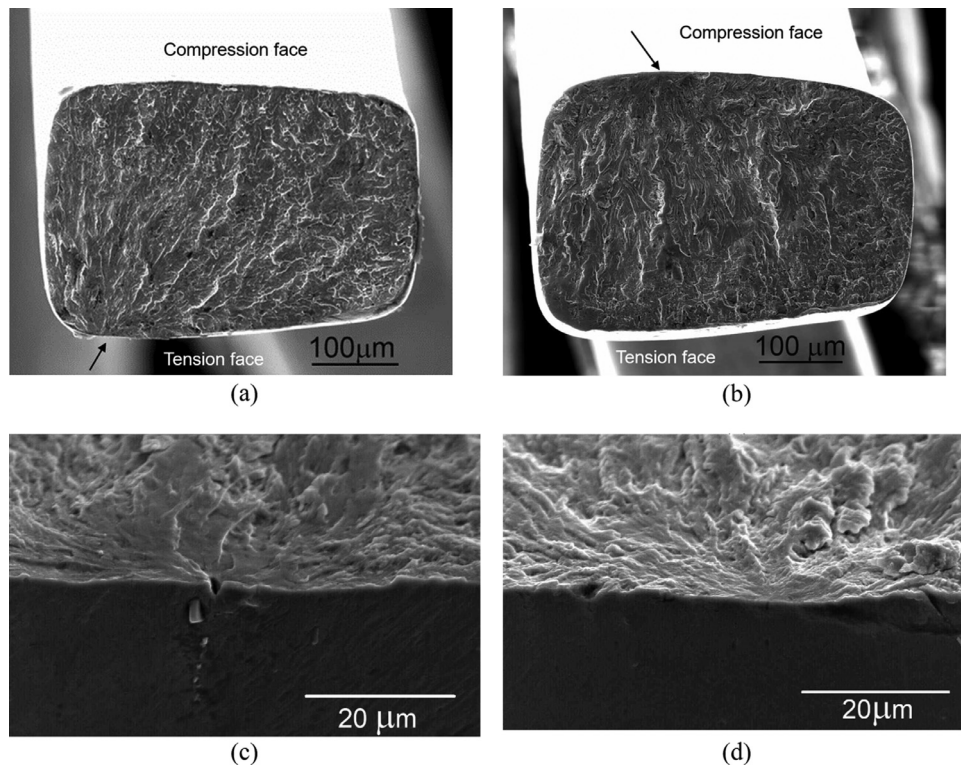


Fig. 14. Scanning electron microscopy fractography of fatigue fractured specimens where the black arrows in (a) and (b) indicate the crack initiation locations. Fatigue crack nucleation (a) from the tensile face for a case where the load ratio, R , is positive, and (b) for a case where the load ratio, R , is negative, from the compression side of the bend specimen. (c) High magnification of crack initiation from an inclusion. (d) Fatigue fracture surface where no apparent inclusion or defect is present.

strain amplitude versus mean strain, at 90% reliability and 95% confidence, is thus monotonic up to a mean strain of 8%, and is composed of a segment with a negative slope and a segment that has zero slope. This is in contrast to many constant life diagrams for Nitinol in the literature, as they are often non-monotonic. The allowable strain amplitude for 90% reliability to 400×10^6 cycles of straining with 95% confidence at mean strains of the order of 2% to 3% is in the range 0.25% to 0.16%. We conclude that the notion that increasing the mean strain will increase, or at least have no negative effect on, fatigue lifetimes in Nitinol is highly questionable, and may actually be erroneous for mean strains up to 8%. Our results are of some significance as medical grade Nitinol is often operated *in vivo* in conditions where the mean strain is of the order of 2% or perhaps higher.

Declaration of Competing Interest

The authors declare that they have no known competing financial interests or personal relationships that could have appeared to influence the work reported in this paper.

CRediT authorship contribution statement

Hengchu Cao: Conceptualization, Investigation, Writing - original draft, Writing - review & editing. **Ming H. Wu:** Supervision. **Fei Zhou:** Formal analysis. **Robert M. McMeeking:** Formal analysis, Validation, Writing - original draft, Writing - review & editing. **Robert O. Ritchie:** Validation, Writing - original draft, Writing - review & editing.

Acknowledgement

This research was supported by [Edwards Lifesciences](#).

Appendix A. Statistical analysis of very high-cycle fatigue life data

Using the procedure described below, a preliminary statistical analysis was performed using all the test data to estimate the 50% reliability boundary. Those specimens tested under conditions that fell above the 50% reliability boundary were

excluded from the subsequent statistical analysis to better define the lower-bound failure envelop for the effective fatigue strain amplitude for 90% reliability at a 95% confidence level. Specifically, we eliminated from the data those that lie above the dashed lines in Fig. 11. The omission of these data had little effect on the constant life model for 400×10^6 cycles because the large majority of these failures occurred at many fewer load applications, and at much higher strain amplitudes, than those ultimately associated with the constant life model for 400×10^6 cycles. A further justification for omitting the low-cycle fatigue data from our statistical model of the high-cycle behavior of Nitinol is that fatigue life S - N curves for metals usually exhibit a transition between the low-cycle and high-cycle regimes that often requires separate fitting to power laws that have exponents that are significantly different from each other. Therefore, it is likely that the model for the high-cycle fatigue regime that is our objective will not be less accurate and, if anything, will be probably more accurate, as a result of omission of the low-cycle fatigue data.

With the assumptions previously described in the body of this paper, we identify a Weibull (1961) model for the distribution of fatigue fractures such that the fraction of specimens, $\Phi = 1 - \rho$, that have fractured under combined fatigue strain amplitude ε_a and mean strain of ε_m by N cycles of straining is given by:

$$\Phi = 1 - \exp\left\{-\left[KN(\varepsilon_a + \xi\varepsilon_m)^n\right]^\beta\right\} \quad (\text{A1})$$

where K , ξ , n and β are model parameters to be determined. Thus, the probability distribution function for fracture of the specimens is given by:

$$f = \frac{\partial\Phi}{\partial N} = \frac{\beta\left[KN(\varepsilon_a + \xi\varepsilon_m)^n\right]^\beta}{N} \exp\left\{-\left[KN(\varepsilon_a + \xi\varepsilon_m)^n\right]^\beta\right\} \quad (\text{A2})$$

As a first step we proceed to obtain values of the parameters K , ξ , n and β by the maximum likelihood method. The data for the life of specimen i are assigned the designations N_i , ε_{ai} and ε_{mi} for the number of cycles until failure, the strain amplitude and the mean strain, respectively. The likelihood, L_i , of each specimen fracturing, from Eq. (A2), is then:

$$L_i = \frac{\beta\left[KN_i(\varepsilon_{ai} + \xi\varepsilon_{mi})^n\right]^\beta}{N_i} \exp\left\{-\left[KN_i(\varepsilon_{ai} + \xi\varepsilon_{mi})^n\right]^\beta\right\} \quad (\text{A3})$$

In the case of runouts, the likelihood value, L_j , is computed from:

$$L_j = \exp\left\{-\left[KN_j(\varepsilon_{aj} + \xi\varepsilon_{mj})^n\right]^\beta\right\} \quad (\text{A4})$$

where, in this case, $N_j = N_L = 400 \times 10^6$.

The likelihood, L , of the entire data set is the product of all such terms in Eqs. (A3) and (A4). The logarithm, Λ , of this likelihood is then given by:

$$\Lambda(K, \xi, n, \beta) = \ln L = \sum_{i=1}^{n_F} \ln L_i + \sum_{j=1}^{n_R} \ln L_j \quad (\text{A5})$$

where n_F is the number of fractured fatigue specimens, and n_R is the number of runouts included in the analysis. We then maximize Λ with respect to the parameters K , ξ , n and β , and evaluate them as K^* , ξ^* , n^* and β^* , respectively, that provide the maximum of Λ , which we designate as Λ^* . We carry out this procedure for both the low mean strain regime ($\varepsilon_m < 3\%$) and the high mean strain regime ($\varepsilon_m > 3\%$), with $\xi = 0$ in the latter case. The computations throughout, including those discussed below, were performed with use of Mathcad (Version 15.0, PTC Inc., Needham, MA). In our treatment of the maximum likelihood function and the confidence intervals (see below), we found that outcomes are more consistent with the Nitinol fatigue data when we use the same exponent n^* for both the low and high mean strain regimes. Results for K^* , ξ^* , n^* and β^* are provided in Table A1, along with the resulting effective fatigue strain amplitudes for a life of 400×10^6 cycles, where strain is measured in %.

One option is to use the point estimates K^* , ξ^* , n^* and β^* as the most probable values for the parameters K , ξ , n and β and utilize these point estimates to deduce the fatigue reliability model. To achieve this, we first substitute Eq. (4) and the

Table A1

Maximum likelihood estimates of Weibull parameters and exponents as well as resulting effective fatigue strain amplitudes for a life of 400×10^6 cycles.

Parameter	Low Mean Strain Regime $\varepsilon_m < 3\%$	High Mean Strain Regime $\varepsilon_m > 3\%$
K^*	3.5×10^{-8}	2.6×10^{-3}
ξ^*	0.13	0
n^*	10	10
β^*	1.23	0.65
ε_e^*	0.64%	0.18%
$\bar{\varepsilon}_e$	0.55%	0.16%

point estimates K^* , n^* and β^* into Eq. (A1) to obtain, after rearrangement,

$$\varepsilon_e = \left[\frac{\left(\ln \frac{1}{\rho}\right)^{\frac{1}{\beta^*}}}{K^* N} \right]^{\frac{1}{n^*}} \tag{A6}$$

where N in this expression is the number of cycles survived with reliability ρ at an effective fatigue strain amplitude ε_e . As we seek a constant life model for reliability $\rho = \rho_R (\equiv 0.9)$ for a life of $N = N_L (\equiv 400 \times 10^6)$ cycles, we substitute these values into Eq. (A6) and obtain the effective fatigue strain amplitude for such reliability and life as:

$$\varepsilon_e^* = \left[\frac{\left(\ln \frac{1}{\rho_R}\right)^{\frac{1}{\beta^*}}}{K^* N_L} \right]^{\frac{1}{n^*}} \tag{A7}$$

The resulting values for ε_e^* are provided in Table A1, and the associated constant life model, for 90% reliability for a life of 400×10^6 cycles, is then obtained from Eq. (4) as:

$$\varepsilon_a + \xi^* \varepsilon_m = \varepsilon_e^* \tag{A8}$$

As is common practice, we exploit confidence intervals to take one step further to obtain a fatigue reliability model at a specified confidence level. We use the likelihood ratio interval method for this purpose, and, at the specified confidence level, seek the most conservative lower bound on the effective fatigue strain amplitude. To do this, we convert the functional dependence of the logarithmic likelihood from K , ξ , n and β as used in Eq. (A5) to dependence on ε_e^L , ξ , n and β so that:

$$\Lambda = \Lambda(\varepsilon_e^L, \xi, n, \beta) \tag{A9}$$

where ε_e^L is the effective fatigue strain amplitude permitting a lifetime of N_L cycles of straining with ρ_R reliability. This step is achieved by writing the parameter K in terms of ε_e^L through modification of Eq. (A7) to read:

$$K = \frac{\left(\ln \frac{1}{\rho_R}\right)^{\frac{1}{\beta}}}{N_L (\varepsilon_e^L)^n} \tag{A10}$$

We then substitute Eq. (A10) into Eqs. (A3) and (A4). As a result, the likelihood, L , becomes a function of ε_e^L , ξ , n and β instead of K , ξ , n and β . This can be understood through consideration of Eq. (A3), where the likelihood of fractured specimen i becomes:

$$L_i = \left[\frac{N_i}{N_L} \left(\frac{\varepsilon_{ai} + \xi \varepsilon_{mi}}{\varepsilon_e^L} \right)^n \right]^\beta \frac{\beta \ln \frac{1}{\rho_R}}{N_i} \exp \left\{ - \left[\frac{N_i}{N_L} \left(\frac{\varepsilon_{ai} + \xi \varepsilon_{mi}}{\varepsilon_e^L} \right)^n \right]^\beta \ln \frac{1}{\rho_R} \right\} \tag{A11}$$

An equivalent expression is obtained from Eq. (A4) for a runout.

With the logarithmic likelihood now a function of ε_e^L , ξ , n and β as in Eq. (A9), the maximized logarithmic likelihood, Λ^* , is such that:

$$\Lambda^* = \Lambda(\varepsilon_e^*, \xi^*, n^*, \beta^*) \tag{A12}$$

We then consider the likelihood, $\Lambda(\varepsilon_e^L, \xi, n, \beta)$, maximized with respect to ξ , n and β but not with respect to ε_e^L , and designate the resulting function of ε_e^L to be $\Lambda_\varepsilon^*(\varepsilon_e^L)$. The difference between Λ^* and Λ_ε^* is known to obey, approximately, chi square statistics with 1 degree of freedom such that (Nelson, 1990):

$$\Lambda^* - \Lambda_\varepsilon^*(\varepsilon_e^L) \geq \frac{1}{2} \chi^2(\nu, 1) \tag{A13}$$

where $\chi^2(\nu, 1)$ is the critical value (sometimes known as chi square percentile) for a chi square distribution of degree of freedom 1 at a fractional probability ν (Nelson, 1990; Meeker and Escobar, 1998). Thus, if we solve for ε_e^L from:

$$\Lambda_\varepsilon^*(\varepsilon_e^L) = \Lambda^* - \frac{1}{2} \chi^2(\nu, 1) \tag{A14}$$

for a specific value of ν , there is a probability ν that, upon repeated testing to obtain fatigue data, the resulting maximum likelihood value of ε_e^L will lie within the range ε_e^- to ε_e^+ where $\varepsilon_e^- < \varepsilon_e^*$ and $\varepsilon_e^+ > \varepsilon_e^*$ are the two solutions for ε_e^L from Eq. (A14) (Meeker and Escobar, 1998). For a one-sided interval with fractional probability δ , we assume symmetry about ε_e^* and thus that half of the testing campaigns undertaken will lead to a maximum likelihood for ε_e^L that will lie to one side of ε_e^* and that the fraction $\nu/2$ of the testing campaigns will lead to a maximum likelihood for ε_e^L that will lie on the other side of ε_e^* . Thus, $2\delta = \nu + 1$, and for a one-sided confidence interval at probability δ we solve the equivalent of Eq. (A14) in the form:

$$\Lambda_\varepsilon^*(\varepsilon_e^L) = \Lambda^* - \frac{1}{2} \chi^2(2\delta - 1, 1) \tag{A15}$$

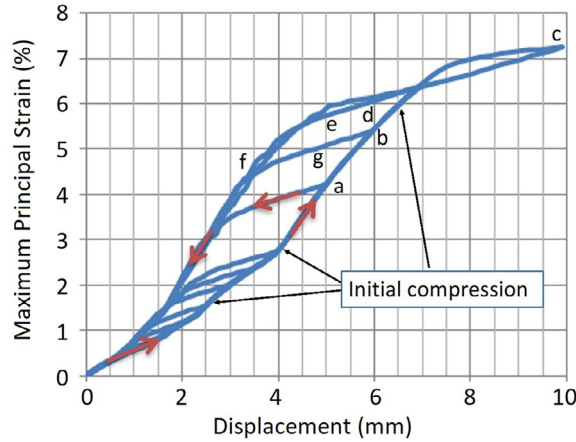


Fig. B1. Plot of the maximum principal strain in the fatigue specimen as a function of the displacement of one end tab towards the other as computed by the finite element method. The line on the right with the red upward pointing arrows is the result when the specimen is being compressed from the origin to the point on the diagram marked c. This line is marked as “Initial compression.” The line on the left with the steeply red downward pointing arrow is the result after compression to c followed by re-extension of the specimen. The connecting lines in between these 2 curves, such as the connecting line bf, are results for re-extension of the specimen after limited compression of the specimen. For example, the line marked by b and f is the result for initial compression to b followed by re-extension to f. That line is also the result for initial compression to c followed by re-extension to f and then re-compression to b. The connecting lines are thus those that are followed by the results when the specimen is subject to cyclic strain. Therefore, an example of a result for cyclic straining is compression to c, re-extension to f and then repeated traversing from f to b to f.

and choose the solution for ε_e^L to be the value ε_e^- as it gives the most conservative interpretation of the fatigue data. We carry out this computation for $\delta = 0.95$ and thus achieve 95% confidence, designating this result for the confidence interval on ε_e^L to be $\bar{\varepsilon}_e$. Again, we carry out the procedure for both the low ($\varepsilon_m < 3\%$) and high ($\varepsilon_m > 3\%$) mean strain regimes. The resulting values for $\bar{\varepsilon}_e$ are provided in Table A1.

The associated lower bound constant life model for survival to 400×10^6 cycles with 90% reliability at 95% confidence is then obtained from Eq. (4) as:

$$\varepsilon_a + \xi^* \varepsilon_m = \bar{\varepsilon}_e \quad (\text{A16})$$

As this result is a more conservative version of the constant life model than Eq. (A8), we plot Eq. (A16) in Fig. 11, and do so for both the low ($\varepsilon_m < 3\%$) and high ($\varepsilon_m > 3\%$) mean strain regimes.

Consistent with the results in Eq. (A16), from the equivalent of Eq. (A6) we obtain a model for lower bound strain-life (S-N) plots at 90% reliability with 95% confidence as:

$$\varepsilon_e = \left(\frac{N_L}{N} \right)^{\frac{1}{n^*}} \bar{\varepsilon}_e \quad (\text{A17})$$

We consider the model in Eq. (A17) to give a lower bound on the effective fatigue strain amplitude as a function of N , and plots of Eq. (A17) are shown in Fig. 13 for both the low ($\varepsilon_m < 3\%$) and high ($\varepsilon_m > 3\%$) mean strain regimes.

Appendix B. An erroneous calibration of the fatigue specimen and the resulting misleading constant life diagram

Pelton et al. (2008) describe analysis of a diamond strut Nitinol fatigue specimen by the finite element method. Although they present some calibration formulae for the diamond strut specimen in an appendix, their summary is incomplete in regard to precisely how the strain amplitude and the mean strain were computed from the results of their finite element analysis. In the body of the paper and in the appendix, Pelton et al. (2008) present formulae in which the strain in a Nitinol component is a unique function of the boundary displacement imposed on it. However, due to the Nitinol stress-strain hysteresis loop as shown in Fig. 1, the relationship between component strain and imposed boundary displacement is, in reality, path-dependant. Therefore, a possible interpretation of the analysis carried out by Pelton et al. (2008) for their diamond strut Nitinol fatigue specimen is that they computed the strain amplitude and the mean strain during fatigue cycling from a unique relationship between specimen strain and imposed boundary displacement, and therefore omitted the effect of path dependence in that relationship.

To illustrate the consequence and significance of omitting path dependence in the strain calculation for each test condition when developing a constant life diagram for Nitinol fatigue, we undertook an effort to analyse our fatigue data by an erroneous method that uses mean strains and strain amplitudes calculated from a unique relationship between component strain and the imposed boundary displacement. Finite element results for the deformation of our fatigue specimen as depicted in Fig. B1 were utilized, with this figure showing the maximum principal strain, found at the center of the specimen gauge length on the convex side, as a function of specimen compression. The full description of Fig. B1 is given in the figure

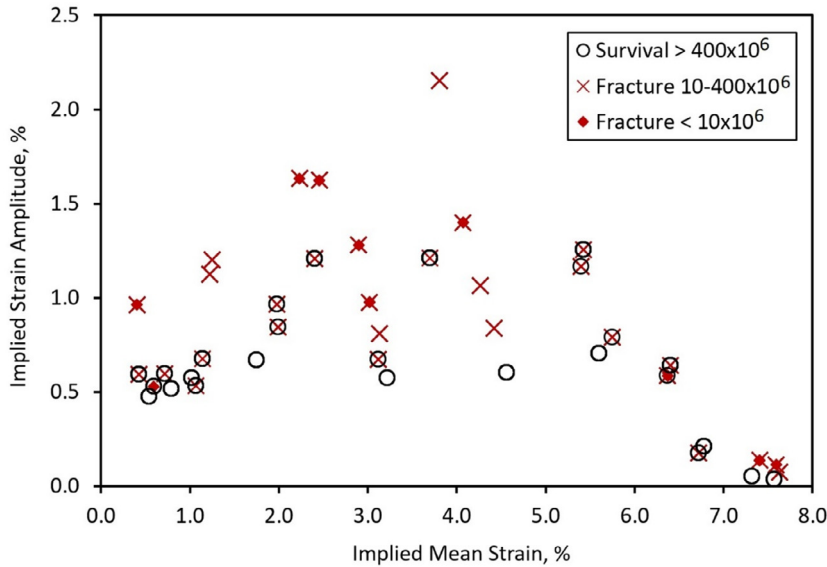


Fig. B2. A faulty Goodman-Haigh diagram for Nitinol fatigue data computed by the erroneous specimen calibration method described in Appendix B. The diagram shows the implied strain amplitude and the implied mean strain for specimens that fractured prior to 10×10^6 cycles, those that fractured between 10×10^6 and 400×10^6 cycles and those that survived without fracture to 400×10^6 cycles (runouts).

caption. In the analysis carried out for this appendix, the strain amplitude and the mean strain for a given range of specimen compression were computed using only the rightmost line in Fig. B1 that gives the relationship between the maximum principal strain in the specimen and its initial compression, i.e., using the line marked ‘Initial compression.’ As a consequence, the effect of strain cycling is neglected when only this rightmost line in Fig. B1 is utilized, and thus the method is erroneous. That is, we compute the strain amplitude and the mean strain from a unique relationship between component maximum principal strain and imposed boundary displacement that is given by the line marked ‘Initial compression,’ and we neglect any path dependence of the relationship.

For example, consider the specimen when it is being cycled between a compression displacement of 5 mm and a compression displacement of 6 mm. In the erroneous method used for this appendix, points a and b in Fig. B1 are used for the computation of the strain amplitude and the mean strain. Point a is at (5 mm, 0.0418) while point b is at (6 mm, 0.0545). Therefore, in the erroneous method, when the specimen is cycled between a compression of 5 mm and 6 mm, the strain amplitude is computed as $(0.0545 - 0.0418)/2 = 0.64\%$ and the mean strain is computed as $(0.0545 + 0.0418)/2 = 4.82\%$.

This erroneous method is used to compute the strain amplitude and the mean strain from our Nitinol fatigue data and the results are plotted in Fig. B2 as a Goodman diagram. We infer constant life models from this plot, but do so only by eye, and observe that such constant life models at 400×10^6 cycles and at 10×10^6 cycles appear to be non-monotonic. Specifically, we deduce that in Fig. B2 the strain amplitude for a fatigue life of 400×10^6 cycles increases from 0.45% at zero mean strain to about 0.7% at a mean strain of 5.6%, but then declines for mean strain exceeding 6%. The non-monotonic nature of this implied constant life model resembles the non-monotonicity in models published by Pelton et al. (2003, 2008). However, the constant life model implied by the results in Fig. B2 is erroneous because of the errors in the computation of the strain amplitude and the mean strain. We conclude that comparable errors may have occurred in the development of the constant life model published by Pelton et al. (2003, 2008), and possibly in those published elsewhere, and, therefore, such constant life models are possibly erroneous and misleading. We believe that this source of error is a contributor to some of the differences between some fatigue data previously published for medical implant grade Nitinol and our data in the current paper.

In the context of Fig. B1, we now briefly describe the correct procedure for computing the strain amplitude and the mean strain. We do so for a specimen that has first experienced overstraining by compression from the origin to point c in Fig. B1. The specimen is then allowed to re-extend to the point e in Fig. B1, and thereafter the compression is cycled between 5 mm and 6 mm, implying that the specimen repeatedly traverses e to d to e. The point e is at (5 mm, 0.0568) while the point d is at (6 mm, 0.0605). Therefore, the strain amplitude for such cycling is 0.19% and the mean strain is 5.87%. Thus, the correct result for the strain amplitude is much less than the erroneous result of 0.6%, making it clear that the erroneous result flatters the fatigue durability of the material for the number of cycles of straining that it survives without fracture. Note that a similar correct result for strain amplitude arises in the absence of overstraining, although the mean strain is somewhat different. Say the specimen is compressed from the origin to the point b in Fig. B1 and the compression is then cycled between 6 mm and 5 mm, implying that the specimen repeatedly traverses b to g to b. The point g is at (5 mm, 0.0505) while b, as noted above, is at (6 mm, 0.0545). Therefore, the strain amplitude for such cycling is 0.20% and the mean

strain is 5.25%. Thus, the correct result for the strain amplitude is much less than the erroneous result of 0.6%, making it clear that this erroneous result also flatters the fatigue durability of the material for the number of cycles of straining that it survives without fracture. Also, note that the strain amplitude without overstraining is very similar to the result with overstraining, an outcome associated with the fact that the strain amplitude reflects incrementally linear elastic behavior. This provides further confirmation that our calibration results for strain amplitude tend to be relatively accurate, even if the mean strain has errors.

We note also that the discrepancies described in this appendix tend to be most severe in the intermediate range of strains from 1% to 6%, indicating that the robustness of Nitinol's fatigue durability will be exaggerated in this range of strains if the erroneous method is utilized for computing the strain amplitude and mean strains. This observation is consistent with the non-monotonic features of constant life models published by Pelton et al. (2003, 2008). We can infer from this exercise that the "apparent" increase in strain amplitude limit in the intermediate range of mean strain (1% to 6%) in some constant life models that have been published is probably due primarily to erroneous fatigue strain calculations when converting from cyclic imposed displacements.

References

- Auricchio, F., Taylor, R.L., 1997. Shape-memory alloys: modelling and numerical simulations of the finite-strain superelastic behavior. *Comput. Methods Appl. Mech. Eng.* 143, 175–194.
- Auricchio, F., Taylor, R.L., Lubliner, J., 1997. Shape-memory alloys: macromodelling and numerical simulations of the superelastic behavior. *Comput. Methods Appl. Mech. Eng.* 146, 281–312.
- Basquin, O.H., 1910. The exponential law of endurance tests. *ASTM Proc.* 10, 625–630.
- Cheng, C.P., Wilson, N.M., Hallett, R.L., Herfkens, R.J., Taylor, C.A., 2006. In vivo MR angiographic quantification of axial and twisting deformations of the superficial femoral artery resulting from maximum hip and knee flexion. *J. Vasc. Interv. Radiol.* 17, 979–987.
- Coffin, L.E., 1954. A study of the effect of cyclic thermal stresses on ductile metal. *Trans. ASME* 76, 931–950.
- Duerig, T.W., Melton, K.N., Stöckel, D., Wayman, C.M., 1990. *Engineering Aspects of Shape Memory Alloys*. Butterworth-Heinemann, London.
- Duerig, T., Pelton, A., Stoelckel, D., 1999. An overview of nitinol medical applications. *Mater. Sci. Eng. A* A273–A275, 149–160.
- Grassi, C.J., 1991. Inferior vena cava filters: analysis of five currently available devices. *Am. J. Radiol.* 156, 813–821.
- Gupta, S., Pelton, A.R., Weaver, J.D., Gong, X.-Y., Nagarajaa, S., 2015. High compressive pre-strains reduce the bending fatigue life of nitinol wire. *J. Mech. Behav. Biomed. Mater.* 44, 96–108.
- Harlow, D., Cao, H., Schmidt, P., 2016. Statistical modeling of high cycle fatigue with censored data. *Mater. Perform. Charact.* 5, 364–372.
- Hertzberg, R.W., 1996. *Deformation and Fracture Mechanics of Engineering Materials*, 4th ed John Wiley and Sons, New York.
- Hull, J.E., Robertson, S.W., 2009. Bard Recovery filters: evaluation and management of vena cava limb perforation, fracture and migration. *J. Vasc. Interv. Radiol.* 20, 52–60.
- Jiang, D., Kyriakides, S., Bechle, N.J., Landis, C.M., 2017. Bending of pseudoelastic NiTi tubes. *Int. J. Solids Struct.* 124, 192–214.
- Kim, Y., Miyazaki, S., 1997. Fatigue life of Ti-50 at% Ni and Ti-40Ni-10Cu (at%) shape memory alloy wires. In: *Proceedings of the Second International Conference on 'SMST'*, Asilomar CA. International Organization on SMST, pp. 473–478 March 1997.
- Laborda, A., Sierre, S., Malvé, M., De Blas, I., Ioakeim, I., Kuo, W.T., De Gregorio, M.A., 2014. Influence of breathing movements and Valsalva maneuver on vena caval dynamics. *World J. Radiol.* 6, 833–839.
- Lanz, J., Kim, W.-K., Walther, T., Burgdorf, C., Möllmann, H., Linke, A., Redwood, S., Thilo, C., Hilker, M., Joner, M., Thiele, H., Conzelmann, L., Conradi, L., Kerber, S., Schymik, G., Prendergast, B., Husser, O., Stortecky, S., Heg, D., Jüni, P., Windecker, S., Pilgrim, T., 2019. Safety and efficacy of a self-expanding versus a balloon-expandable bioprosthesis for transcatheter aortic valve replacement in patients with symptomatic severe aortic stenosis: a randomised non-inferiority trial. *Lancet North Am. Ed.* 394, 1619–1628.
- Mao, S.C., Han, X.D., Tian, Y.B., Luo, J.F., Zhang, Z., Ji, Y., Wu, M.H., 2008. In situ EBSD investigations of the asymmetric stress-induced martensitic transformation in TiNi shape memory alloys under bending. *Mater. Sci. Eng. A* 498 (1), 278–282.
- Meeker, W.Q., Escobar, L.A., 1998. *Statistical Methods for Reliability Data*. John Wiley & Sons, New York.
- Meyer, P.L., 1965. *Introduction to Probability and Statistical Applications*. Addison-Wesley, Reading, MA.
- Milnor, W.R., 1982. *Hemodynamics*. Williams & Wilkins, Baltimore.
- Mitchell, M.R., 1996. Fundamentals of modern fatigue analysis for design. In: *ASM Handbook: Fatigue and Fracture*. ASM International, West Conshohocken PA, pp. 227–262.
- Miyazaki, S., Mizukoshi, K., Ueki, T., Sakuma, T., Liu, Y., 1999. Fatigue life of Ti-50 at% Ni and Ti-40Ni-10Cu (at%) shape memory alloy wires. *Mater. Sci. Eng. A* 273–275, 658–663.
- Morgan, N.B., Painter, J., Moffat, A., 2003. Mean strain effects and microstructural observations during *in vitro* fatigue testing of NiTi. In: *Proceedings of the International Conference on 'SMST'*. International Organization on SMST, Pacific Grove CA, pp. 303–310 May 2003.
- Murphy, E.H., Johnson, E.D., Arko, F.R., 2008. Evaluation of wall motion and dynamic geometry of the inferior vena cava using intravascular ultrasound: implications for future device design. *J. Endovasc. Ther.* 15, 349–355.
- Nelson, W., 1990. *Accelerated Testing: Statistical Models, Test Plans and Data Analysis*. John Wiley & Sons, New York.
- Otsuka, K., Ren, X., 2005. Physical metallurgy of Ti-Ni-based shape memory alloys. *Prog. Mater. Sci.* 50, 511–678.
- Pelton, A.R., 2011. Nitinol fatigue: a review of microstructures and mechanisms. *J. Mater. Eng. Perform.* 20, 613–617.
- Pelton, A.R., DiCello, J., Miyazaki, S., 2000. Optimisation of processing and properties of medical-grade Nitinol wire. *Minim. Invasive Ther. Allied Technol.* 9, 107–119.
- Pelton, A.R., Gong, X.-Y., Duerig, T.W., 2003. Fatigue testing of diamond-shaped specimens. In: *Proceedings of the International Conference on 'SMST'*. International Organization on SMST, Pacific Grove CA, pp. 293–302 May 2003.
- Pelton, A.R., Schroeder, V., Mitchell, M.R., Gong, X.-Y., Barney, M., Robertson, S.W., 2008. Fatigue and durability of nitinol stents. *J. Mech. Behav. Biomed. Mater.* 1, 153–164.
- Reinoehl, M., Bradley, D., Bouthot, R., Proft, J., 2000. The influence of melt practice on final fatigue properties of superelastic NiTi wires. In: *Proceedings of the International Conference on 'SMST'*. International Organization on SMST, Pacific Grove CA, pp. 397–403 April-May 2000.
- Robertson, S.W., Pelton, A.R., Ritchie, R.O., 2012. Mechanical fatigue and fracture of Nitinol. *Int. Mater. Rev.* 57, 1–36.
- Schmidt, P.A., Krams, W.E., Cao, H., 2019. Application of classical fatigue and fatigue-to-fracture techniques for very-high-cycle life qualification of cardiac devices. In: *Mitchell, M.R., Berg, B.T., Woods, T.O., Jerina, K.L. (Eds.), Fourth Symposium on Fatigue and Fracture of Metallic Medical Materials and Devices*. ASTM International, West Conshohocken PA, pp. 148–163.
- Senthilnathan, K., Shamimi, A., Bonsignore, C., Paranjape, H., Duerig, T., 2019. Effect of prestrain on the fatigue life of superelastic Nitinol. *J. Mater. Eng. Perform.* 28, 5946–5958.
- Shanmugam, V., Zhao, T., Krams, W.E., Joshi, A., Cao, H., Schmidt, P., 2019. Fatigue reliability analysis framework for medical devices based on a probabilistic finite element approach. In: *Mitchell, M.R., Berg, B.T., Woods, T.O., Jerina, K.L. (Eds.), Fourth Symposium on Fatigue and Fracture of Metallic Medical Materials and Devices*. ASTM International, West Conshohocken, PA, pp. 132–147.

- Sheriff, J., Pelton, A.R., Pruitt, L.A., 2004. Hydrogen effects on nitinol fatigue. In: Proceedings of the ASM Materials and Processes for Medical Devices Conference, Minneapolis MN. ASM International, pp. 38–43 August 2004.
- Stöckel, D., Pelton, A.R., Duerig, T., 2004. Self-expanding Nitinol stents: material and design considerations. *Eur. Radiol.* 14, 292–301.
- Stulen, F.B., 1965. Fatigue life data displayed by a single quantity relating alternating and mean stress, technical report AFML-TR-65-121, Air Force Materials Laboratory, Wright-Patterson Air Force Base OH.
- Suresh, S., 1998. *Fatigue of Materials*. Cambridge University Press, Cambridge.
- Tabanli, R.M., Simha, N.K., Berg, B.T., 1999. Mean stress effects on fatigue of NiTi. *Mater. Sci. Eng. A* 273–275, 644–648.
- Tabanli, R.M., Simha, N.K., Berg, B.T., 2001. Mean strain effects on the fatigue properties of superelastic NiTi. *Metall. Mater. Trans. A* 32A, 1866–1869.
- Tolomeo, D., Davidson, S., Santinoranout, M., 2000. Cyclic properties of superelastic nitinol: design implications. In: Proceedings of the International Conference on "SMST". International Organization on SMST, Pacific Grove CA, pp. 471–476 April-May 2000.
- Tripathy, S., Wu, M., Cao, H., 2019. Finite element framework for fatigue performance assessment of superelastic Nitinol used in medical devices. In: Mitchell, M.R., Berg, B.T., Woods, T.O., Jerina, K.L. (Eds.), *Fourth Symposium on Fatigue and Fracture of Metallic Medical Materials and Devices*. ASTM International, West Conshohocken PA STP 1616.
- Weibull, W., 1961. *Fatigue Testing and Analysis of Results*. Pergamon Press, New York.
- Wick, A., Gong, X.-Y., Fino, J., Sheriff, J., Pelton, A.R., 2004. Bending fatigue characteristics of nitinol. In: Proceedings of the ASM Materials and Processes for Medical Devices Conference, Minneapolis MN. ASM International, pp. 15–20 August 2004.